The Astrophysical Journal, 826:175 (17pp), 2016 August 1 doi:10.3847/0004-637X/826/2/175

THE IONIZED GAS IN NEARBY GALAXIES AS TRACED BY THE [N II] 122 AND 205 μm TRANSITIONS

R. Herrera-Camus[1,2], A. Bolatto[1], J. D. Smith[3], B. Draine[4], E. Pellegrini[5], M. Wolfire[1], K. Croxall[6], I. de Looze[7], D. Calzetti[8], R. Kennicutt[7], A. Crocker[9], L. Armus[10], P. van der Werf[11], K. Sandstrom[12], M. Galametz[13], B. Brandl[11,14], B. Groves[15], D. Rigopoulou[16], F. Walter[17], A. Leroy[6], M. Boquien[7], F. S. Tabatabaei[18], and P. Beirao[19]
[1] Department of Astronomy, University of Maryland, College Park, MD 20742, USA
[2] Max-Planck-Institut für extraterrestrische Physik, Giessenbachstr., D-85748 Garching, Germany
[3] Department of Physics and Astronomy, University of Toledo, 2801 West Bancroft Street, Toledo, OH 43606, USA
[4] Department of Astrophysical Sciences, Princeton University, Princeton, NJ 08544, USA
[5] Zentrum für Astronomie der Universität Heidelberg, Institut für Theoretische Astrophysik, Albert-Ueberle-Str. 2, D-69120 Heidelberg, Germany
[6] Department of Astronomy, The Ohio State University, 4051 McPherson Laboratory, 140 West 18th Avenue, Columbus, OH 43210, USA
[7] Institute of Astronomy, University of Cambridge, Madingley Road, Cambridge, CB3 0HA, UK
[8] Department of Astronomy, University of Massachusetts, Amherst, MA 01003, USA
[9] Department of Physics, Reed College, Portland, OR 97202, USA
[10] Spitzer Science Center, California Institute of Technology, MC 314-6, Pasadena, CA 91125, USA
[11] Leiden Observatory, Leiden University, P.O. Box 9513, 2300 RA Leiden, The Netherlands
[12] Center for Astrophysics and Space Sciences, Department of Physics, University of California, San Diego, 9500 Gilman Drive, La Jolla, CA 92093, USA
[13] European Southern Observatory, Karl Schwarzschild Strasse 2, D-85748 Garching, Germany
[14] Delft University of Technology, Faculty of Aerospace Engineering, Kluyverweg 1, 2629 HS Delft, The Netherlands
[15] Research School of Astronomy & Astrophysics, Australian National University, Canberra, ACT 2611, Australia
[16] Department of Physics, University of Oxford, Keble Road, Oxford OX1 3RH, UK
[17] Max-Planck-Institut für Astronomie, Königstuhl 17, D-69117 Heidelberg, Germany
[18] Instituto de Astrofísica de Canarias, C/Vía Láctea, s/n, E-38205, San Cristóbal de La Laguna, Tenerife, Spain
[19] Observatoire de Paris, 61 avenue de l'Observatoire, F-75014 Paris, France
Received 2015 October 29; revised 2016 May 10; accepted 2016 May 10; published 2016 July 29

ABSTRACT

The [N II] 122 and 205 μm transitions are powerful tracers of the ionized gas in the interstellar medium. By combining data from 21 galaxies selected from the *Herschel* KINGFISH and Beyond the Peak surveys, we have compiled 141 spatially resolved regions with a typical size of ∼1 kpc, with observations of both [N II] far-infrared lines. We measure [N II] 122/205 line ratios in the ∼0.6–6 range, which corresponds to electron gas densities of n_e ∼ 1–300 cm^{-3}, with a median value of $n_e = 30$ cm^{-3}. Variations in the electron density within individual galaxies can be as high as a factor of ∼50, frequently with strong radial gradients. We find that n_e increases as a function of infrared color, dust-weighted mean starlight intensity, and star-formation rate (SFR) surface density (Σ_{SFR}). As the intensity of the [N II] transitions is related to the ionizing photon flux, we investigate their reliability as tracers of the SFR. We derive relations between the [N II] emission and SFR in the low-density limit and in the case of a log-normal distribution of densities. The scatter in the correlation between [N II] surface brightness and Σ_{SFR} can be understood as a property of the n_e distribution. For regions with n_e close to or higher than the [N II] line critical densities, the low-density limit [N II]-based SFR calibration systematically underestimates the SFR because the [N II] emission is collisionally quenched. Finally, we investigate the relation between [N II] emission, SFR, and n_e by comparing our observations to predictions from the MAPPINGS-III code.

Key words: galaxies: ISM – galaxies: star formation – ISM: structure

1. INTRODUCTION

Infrared transitions are a powerful tool for investigating the neutral and ionized gas in the interstellar medium (ISM). At wavelengths greater than 100 μm, the brightest lines in star-forming galaxies are the [C II] 158 μm and the [N II] 122 and 205 μm fine-structure transitions (Wright et al. 1991; Bennett et al. 1994; Malhotra et al. 2001; Brauher et al. 2008; Zhao et al. 2013, 2016). While the [C II] line arises from both the neutral and the ionized gas, the ionization potential of nitrogen is about ∼0.9 eV higher than that of hydrogen, which implies that [N II] lines originate only from the ionized gas. This, combined with the fact that far-infrared lines are affected by dust only in extreme cases, makes the [N II] 122 and 205 μm transitions a powerful means to study the properties of the ionized ISM.

The pair of infrared [N II] lines is the result of the splitting of the ground state of N^+ into three fine-structure levels. These levels are excited primarily by electron collisions, and the critical densities (n_{crit}) for the resulting [N II] 121.89 μm ($^3P_2 \rightarrow {}^3P_1$) and [N II] 205.19 μm ($^3P_1 \rightarrow {}^3P_0$) transitions are 290 cm^{-3} and 44 cm^{-3}, respectively (assuming $T \approx 8000$ K; Hudson & Bell 2004). These excitation conditions imply that the [N II] 205 μm power per N^+ scales linearly with electron density (n_e) up to ∼10 cm^{-3}, growing increasingly more slowly with n_e until leveling off at n_e ∼ 60–70 cm^{-3} (e.g., see Figure 8 in Langer et al. 2015). Above n_e ∼ 10 cm^{-3}, the [N II] 122/205 μm line ratio starts to increase from its base value of ∼0.6 (Tayal 2011) as a function of n_e, until the electron density of the gas approaches the critical density of the [N II] 122 μm line. As we show in Figure 4, [N II]-based n_e measurements of the photoionized gas have been made for the Galactic plane (Bennett et al. 1994; Goldsmith et al. 2015), (ultra)luminous infrared galaxies ((U)LIRGs) (Zhao et al. 2016), and a handful of other sources: M82 (∼180 cm^{-3}, Petuchowski et al. 1994), the Carina nebula (∼28 cm^{-3}, Oberst et al. 2006, 2011), the central region of NGC 1097 (∼160 cm^{-3}, Beirão et al. 2012), M51 (∼8 cm^{-3}, Parkin et al. 2013), NGC 891 (∼10–100 cm^{-3}, Hughes et al.

2014), and the central region of IC 342 ($\sim$110 cm^{-3}, Rigopoulou et al. 2013).

Another interesting application of the [N II] far-infrared (FIR) lines is to use them as tracers of star-formation activity. This use is motivated by the fact that the [N II] lines arise from gas ionized by O and early-B type stars, thus providing a direct measurement of the ionizing photon rate, which is directly related to the star-formation rate (SFR) (Bennett et al. 1994; McKee & Williams 1997). The other advantage is that the [N II] far-infrared line emission can be observed in high-redshift galaxies by ground-based observatories like the Atacama Large Millimeter Array (Ferkinhoff et al. 2011, 2015; Combes et al. 2012; Decarli et al. 2012; Nagao et al. 2012). Empirical calibrations of the SFR based on [N II] 122 and 205 μm luminosities have been derived based on observations of nearby galaxies (e.g., M83, M51, NGC 891; Wu et al. 2015; Hughes et al. 2016) and samples of star-forming galaxies and (U)LIRGs by Farrah et al. (2013) and Zhao et al. (2013, 2016). These calibrations provide SFR estimates with an uncertainty of a factor of $\sim$3 for star-forming galaxies with infrared luminosities below $\sim 10^{11.5}$ $L_{\odot}$; for more luminous galaxies, these calibrations tend to underestimate the SFR by factors that can be as high as $\sim$10. On the modeling side, Orsi et al. (2014), based on the "Semi-analytic Galaxies" model (Cora 2006; Orsi et al. 2014) and the photoionization code MAPPINGS-III (Kewley et al. 2001; Groves et al. 2004), studied the evolution of the correlation between the [N II] 205 μm luminosity and SFR from redshift $z = 5$ to the present. They find a [N II]–SFR correlation that is consistent, within the scatter, with the results from Zhao et al. (2013).

One the most important limitations for using the [N II] emission as a star-formation tracer is the decrease in the ratio between the [N II] lines and the FIR luminosity (which is proportional to the SFR) observed in some local and high-redshift galaxies (Walter et al. 2009; Fischer et al. 2010; Graciá-Carpio et al. 2011; Decarli et al. 2012, 2014; Farrah et al. 2013; Zhao et al. 2013). This so-called "[N II] deficit" may arise from environments with high ionization parameters where ionizing photons from dusty H II regions are intercepted by dust (Luhman et al. 2003; Graciá-Carpio et al. 2011), an increased fraction of nitrogen in N^{++} and N^{+++} near very-early-type O stars, and the relatively low critical density of the [N II] far-infrared lines (Langer et al. 2015).

Based on a sample of [N II] 122 and 205 μm resolved observations of 21 nearby galaxies by *Herschel*, the goal of this paper is twofold: first, to measure the beam-averaged electron density of the low-excitation H II gas and explore any potential dependence with the environment (metallicity, radiation field strength, and so on), and second, to derive [N II]-based SFR calibrations and study their reliability. This paper is organized as follows. In Section 2 we describe the observations and the sample under investigation. In Section 3 we use the [N II] 122 to 205 μm line ratio to measure electron densities, and we explore the properties of the ionized gas. In Section 4 we investigate the connection between [N II] emission, star-formation activity, and electron density. Finally, in Section 5 we summarize our main conclusions.

2. SAMPLE AND METHODS

Our study focuses on 21 spiral galaxies that are part of the "Key Insights on Nearby Galaxies: A Far-Infrared Survey with *Herschel*" (KINGFISH; P.I. Kennicutt et al. 2011) and "Beyond the Peak" (BtP; P.I. J. D. Smith) samples. Combined, these surveys provide deep photometric and spectroscopic measurements of 20 centrally pointed regions and one extra-nuclear region (NGC 5457). According to their optical spectral properties, 12 of these 21 galaxies show signatures of active galactic nuclei (AGNs) emission (Ho et al. 1997; Moustakas et al. 2010); however, galaxies in the KINGFISH sample have been selected not to have a strong AGN contribution. Our galaxies cover a total infrared (TIR) luminosity range of $L_{\rm TIR} \sim 10^{8.9}$–$10^{10.7}$ $L_{\odot}$ (Dale et al. 2012) and a global metallicity range of $12 + \log({\rm O/H}) \sim 8.1$–$8.9$ for the Pilyugin & Thuan (2005) calibration (PT05) and $12 + \log({\rm O/H}) \sim 8.7$–$9.2$ for the Kobulnicky & Kewley (2004) calibration (KK04) (Moustakas et al. 2010). The SPIRE Fourier Transform Spectrometer (SPIRE-FTS) beam size at 205 μm is 16.″6 (Makiwa et al. 2013); given the range of distances in our sample ($\sim$3.5–30.6 Mpc), we cover a range of spatial resolutions that goes from $\sim$0.3 kpc for NGC 2976 to $\sim$2.5 kpc for NGC 1266, with a median value of $\sim$0.8 kpc. For more information on the properties of the KINGFISH and BtP galaxies, we refer to Table 1 in Kennicutt et al. (2011).

2.1. Spectroscopic Data

Observations of the [N II] 122 μm transition were carried out with the *Herschel* Photodetector Array Camera & Spectrometer (PACS, Poglitsch et al. 2010) on board *Herschel* as part of the KINGFISH survey. The observations were obtained in the Unchopped Mapping mode and reduced using the *Herschel* Interactive Processing Environment (HIPE) version 11.0. The reductions applied the standard spectral response functions and flat-field corrections and flagged instrument artifacts and bad pixels (see Poglitsch et al. 2010; Kennicutt et al. 2011). Transient removal was performed using a custom treatment designed for the KINGFISH pipeline. In-flight flux calibrations were applied to the data. We mitigated the spatial under-sampling of the beam by using a half-pixel dither and then drizzling the maps (details in Kennicutt et al. 2011). We then integrated in velocity the [N II] 122 μm line from the reduced cubes producing moment-zero maps with 2.″3 pixels. The PACS full width at half maximum[20] (FWHM) at 122 μm is $\approx$10″. The calibration uncertainty on PACS is $\sim$20% (Croxall et al. 2013). For a detailed description of the reduction and processing of the KINGFISH FIR spectral maps, we refer to Croxall et al. (2013).

The [N II] 205 μm transition was observed with the SPIRE-FTS (Griffin et al. 2010) as part of the BtP survey. For a detailed description of the reduction and processing of the spectral maps, we refer to Pellegrini et al. (2013) and E. Pellegrini et al. (2016, in preparation). Hereafter, we will refer to the area covered by a single SPIRE-FTS beam as an "individual region." The SPIRE-FTS instrumental spectral resolution is not sufficient to resolve line profiles in BtP. Profile fitting was done with a fixed-width sinc function, where we fit for the line position and peak. Thus the dominant uncertainty in the [N II] 205 μm line flux measurement is in the uncertainty of the peak above the continuum. To estimate the uncertainty in the continuum under the line, we measure the $1-\sigma$ standard deviation in the residual of the fit and take this to be the uncertainty in one spectral element. As the noise pattern in the continuum is correlated (fringe pattern), we scale the

[20] http://herschel.esac.esa.int/Docs/PACS/pdf/pacs_om.pdf

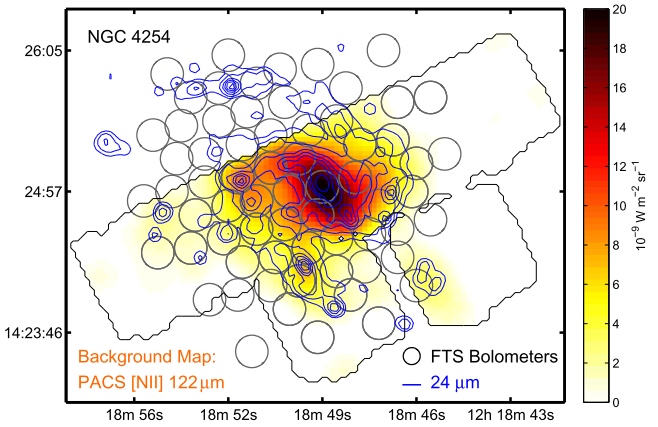

Figure 1. PACS [N II] 122 μm image of NGC 4254. The color scale shows the surface brightness in units of 10^{-9} W m^{-2} sr^{-1}. The black contours delineate the areas where [N II] 122 μm was observed, and the blue contours show the 24 μm dust continuum emission. The gray circles show the distribution of the 17″ SPIRE-FTS bolometers used to detect the [N II] 205 μm line. The axes show the R.A. (J2000) and decl. (J2000) position coordinates.

uncertainty in a single spectral pixel by the number of pixels under an unresolved line to estimate the uncertainty in our fluxes.

The calibration of the SPIRE-FTS spectra depends on the intrinsic source structure. The reduction and calibration routines use gains that are optimized for sources that, compared to the beam size, are either much smaller (point sources) or much more extended. The calibration scale differs by as much as a factor of ∼2 between compact and extended (e.g., see Figure 4 in Wu et al. 2013).

To address the issue of what is the precise gain that needs to be applied to our [N II] 205 μm observations, we compare the SPIRE-FTS synthetic continuum photometry with the SPIRE 250 μm continuum flux from imaging (the synthetic photometry is derived by applying the 250 μm SPIRE filter gain curve to the FTS spectrum). The synthetic and continuum photometry need to match, so we attribute any difference between the two to the gain correction that is due to the intrinsic structure of the source.

Our SPIRE-FTS data were first reduced assuming a point-source distribution. Based on the method described above, we correct our data by scaling the surface brightness at 205 μm of each bolometer by the ratio between the synthetic and imaging photometry at 250 μm. Note that our correction is not based on a constant [N II] 205 μm to continuum ratio, but on the assumption that the gain factor that applies to the 250 μm continuum also applies to the 205 μm data. The typical 250 μm flux of our regions is ∼1.8 Jy, with an uncertainty less than 10% of this value. The mean value of this correction is 1.1.

2.2. Supplementary Data

The supplementary data available includes (1) near- and mid-infrared (24 μm) data from the *Spitzer* Infrared Nearby Galaxy Survey (SINGS; Kennicutt et al. 2003); (2) FIR maps observed with *Herschel* PACS (70, 100, and 160 μm) and SPIRE (250, 350, and 500 μm) drawn from the photometric KINGFISH sample (Dale et al. 2012); and (3) Hα narrow-band images corrected for Galactic extinction, with foreground stars masked and the optical [N II] contribution subtracted (Leroy et al. 2012). The latter are drawn mainly from the SINGS (Kennicutt et al. 2003) and Local Volume Legacy survey (Dale et al. 2009a).

As an example of the data used in this study, Figure 1 shows the [N II] 122 μm surface-brightness map of the spiral galaxy NGC 4254. The blue contours show the 24 μm dust continuum emission, and the gray circles show the spatial distribution of the 68 SPIRE-FTS bolometers used to observe the [N II] 205 μm line emission. For this particular galaxy, the fraction of 205 μm bolometers that overlap the [N II] 122 μm data is 45%. For the entire sample, this fraction is 23%. On the other hand, the overlap between the [N II] spectroscopic data and the complementary photometric data available (e.g., 24 μm, Hα) is nearly complete.

In Section 4 we compare the BtP and KINGFISH data to a sample of local luminous infrared galaxies. This sample consist of 25 ULIRGs observed in [N II] 122 μm emission by Farrah et al. (2013) and 44 (U)LIRGs observed in [N II] 205 μm emission by Zhao et al. (2013) as part of the Great Observatories All-sky LIRG Survey (GOALS; Armus et al. 2009). For these samples of LIRGs, we measure SFRs based on the TIR luminosity (L(8–1000 μm)) and the calibration by Murphy et al. (2011).

2.3. Models

2.3.1. Draine & Li Dust Model

For each BtP galaxy, we have maps of dust properties based on the Draine & Li dust model (DL07; Draine & Li 2007). In brief, the DL07 model considers that dust consists of a combination of carbonaceous and amorphous silicate grains whose grain size distribution and normalization is chosen to match the abundance and average extinction in the Milky Way (Weingartner & Draine 2001). In the model, the dust is heated by a range of radiation fields U, including (1) a diffuse component that is heated by a single radiation field, $U_{\rm min}$; and (2) a more intense component, $U_{\rm min} < U < U_{\rm max}$, that heats dust located near luminous stars (e.g., dust in photodissociation regions heated by OB stars). The dust maps we use in this work are similar to the ones presented in Aniano et al. (2012) and were processed by G. Aniano et al. (2016, in preparation) by fitting the DL07 model to the infrared spectral energy distribution in the 3.6–250 μm wavelength range. The output of the fit includes the dust mass, the dust-weighted mean starlight intensity, $\langle U \rangle$, and the fraction $f_{\rm PDR}$ of the dust luminosity produced by photodissociation regions with $U > 100$.

2.3.2. MAPPINGS-III Photoionization Code

In Section 4 we investigate the relationship between the [N II] emission, the electron density, and the star-formation activity based on the predictions by the shock and photo-ionization code MAPPINGS-III (Kewley et al. 2001; Groves et al. 2004). This code takes synthetic far-ultraviolet (FUV) spectra generated by the Starburst99 code (Leitherer et al. 1999) and produces model H II region spectra integrated over the full ionized volume. The code incorporates a sophisticated treatment of the dust that includes absorption, charging, and photoelectric heating (Groves et al. 2004). The final spectra consist of a set of emission lines that include the [N II] 122 and 205 μm transitions. In this work we use the precomputed grids of MAPPINGS-III generated by Levesque et al. (2010). These grids adopt a wide range of parameters,

including (1) star-formation history (continuous or instantaneous burst), (2) age ($0 \leqslant t_{\rm age} \leqslant 5$ Myr), (3) metallicity ($0.05 \leqslant Z/Z_{\odot} \leqslant 2$), (4) ionization parameter q, which is the ratio between the incident ionizing photon flux and the gas density ($10^7 \leqslant q \leqslant 4 \times 10^8$ cm s^{-1}), and (4) electron density ($n_{\rm e} = 10$ or $100\,{\rm cm}^{-3}$). We use a set of grids that adopt a characteristic ionization parameter for star-forming galaxies of $q = 2 \times 10^7$ cm s^{-1} (Kewley & Dopita 2002), and for a fixed electron density of $n_{\rm e} = 10$ or $100\,{\rm cm}^{-3}$, we allow the metallicity to vary between $Z = Z_{\odot}$ and $Z = 2Z_{\odot}$. We also adopt a continuous star-formation history model at 5 Myr, which corresponds to the age in the Starburst99 model at which there is a balance between the number of O stars being born and dying (Kewley et al. 2001). The SFR calibrations used in this work (Calzetti et al. 2007; Murphy et al. 2011) are also based on Starburst99 calculations that assume a continuous star-formation history model.

2.4. Methods

In order to ensure a proper comparison between the supplementary data and the [N II] 205 μm observations, we convolved all of our maps to match the SPIRE-FTS FWHM at 205 μm using convolution kernels constructed using the methodology of Aniano et al. (2011). We then extracted continuum and line fluxes from regions corresponding to the position and sizes of the SPIRE-FTS [N II] 205 μm data.

In Section 5 we study the reliability of the [N II] far-infrared lines as star-formation tracers. For this purpose, we measure SFR surface densities ($\Sigma_{\rm SFR}$) and SFRs based on a combination of the convolved 24 μm and Hα data following the calibration by Calzetti et al. (2007). This calibration adopts an IMF with $dN/dM \propto M^{-\alpha}$, with $\alpha = -1.3$ in the range 0.1–0.5 $M_{\odot}$ and -2.3 in the range 0.5–120 $M_{\odot}$. This choice of IMF produces SFRs that, for the same number of ionizing photons, are ~14% higher than if we change the upper-mass cutoff to 100 $M_{\odot}$, and a factor 1.59 lower if we assume a Salpeter IMF in the range 0.1–100 $M_{\odot}$.

We also measure TIR luminosities based on the calibration by Galametz et al. (2013) using the 24, 70, 100, and 160 μm convolved data.

For the global metallicities of 17 of the 21 galaxies, we use the average between the KK04 and PT05 "characteristic" metallicities listed in Table 9 of Moustakas et al. (2010). For the four remaining galaxies with metallicity measurements not available in Moustakas et al. (2010), we use oxygen abundances derived from the luminosity–metallicity relation listed in Kennicutt et al. (2011). Nine of the BtP galaxies have measured metallicity gradients (Moustakas et al. 2010). However, the regions in these systems have galactocentric distances $\lesssim 0.3\,R_{25}$ (where R_{25} is the radius of the major axis at the $\mu_B = 25\,{\rm mag\,arcsec}^{-2}$ isophote; de Vaucouleurs et al. 1991; Moustakas et al. 2010), so the effect of the metallicity gradient is small, and we use the central metallicity.

We correct all surface brightnesses and SFR surface densities for inclination by multiplying $\cos(i)$. Inclinations were drawn from the compiled lists in Hunt et al. (2014). We remove NGC 4631 from the analysis due to its high inclination ($i \approx 86°$; Muñoz-Mateos et al. 2009).

3. [N II]-BASED ELECTRON DENSITIES AND THEIR DEPENDENCE ON ENVIRONMENT

3.1. Estimating Ionized Gas Densities from the [N II] Fine-structure Transitions

In this section we discuss how the electron density can be derived from the ratio between the [N II] 122 μm and [N II] 205 μm transitions (from now on the [N II] 122/205 line ratio). Let $f_i(n_{\rm e})$ be the fraction of N^+ in level i, where $i = 0$ is the ground state. The power radiated in the fine-structure lines is

$$L_{\lambda} = \int n({\rm N}^+) P_{\lambda}(n_{\rm e}) dV \quad (1)$$

$$= \left[\frac{{\rm N}^+}{{\rm H}^+}\right] \int n_{\rm e} P_{\lambda}(n_{\rm e}) dV \quad (2)$$

$$P_{205\,\mu{\rm m}}(n_{\rm e}) = f_1(n_{\rm e}) A_{10} h\nu_{10} \quad (3)$$

$$P_{122\,\mu{\rm m}}(n_{\rm e}) = f_2(n_{\rm e}) A_{21} h\nu_{21}, \quad (4)$$

where A_{10} and A_{21} are the Einstein coefficients for the $1 \rightarrow 0$ (205 μm) and $2 \rightarrow 1$ (122 μm) transitions of N^+, respectively. We have calculated $f_i(n_{\rm e})$ for N^+ levels $i = 0,..,4$, using electron collision strengths from Tayal (2011) and radiative decay rates from Galavis et al. (1997) and Storey & Zeippen (2000), for an assumed electron temperature $T = 8000$ K and a range of $n_{\rm e}$. The left panel of Figure 2 shows the variation of the [N II] 122/205 ratio with electron density, $n_{\rm e}$. It can be seen that the line ratio is sensitive to the density of the photoionized gas in the $n_{\rm e} \sim$ 10–1000 cm^{-3} range.

The right-hand panel of Figure 2 shows $P/n_{\rm e}$, where P is the power radiated per N^+ ion, for each individual [N II] transition and for their sum, as a function of the [N II] 122/205 line ratio. This figure illustrates the effect of collisional quenching on the [N II] transitions once the electron density of the gas exceeds the critical density of the line. For example, as the electron density exceeds the critical density of the [N II] 122 μm line, which happens around a line ratio [N II] 122/205 ≈ 5 ($n_{\rm e} \approx 250\,{\rm cm}^{-3}$), the power radiated per ion by the [N II] 122 μm line starts to decrease at a rate comparable to that of the [N II] 205 μm line.

3.2. Distribution of [N II] 122/205 Line Ratios and Electron Densities in the BtP Sample

For 141 individual regions (defined by the area covered by a single SPIRE-FTS beam at 205 μm) for which we have observations of both [N II] transitions with S/N $\geqslant 3$, Figure 3 shows the histogram of the observed [N II] 122/205 line ratios (left panel) and the fraction of the total emitted [N II] 122 μm power per [N II] 122/205 bin (right panel). On the left panel, the two [N II] 122/205 line ratio distributions show the data calibrated as a point source (gray) and after applying the extended emission correction (blue). Both distributions are roughly similar, but the corrected version of the data tends to show higher line ratios. This is the direct result of applying the extended emission correction, which accounts for the overestimation of the [N II] 205 μm intensity when extracted as a point source (see Section 2.1 for details). For the rest of the paper, we base all of the results on the extended-emission-corrected version of the data. The red dashed line shows the line ratio limit of [N II] 122/205 ≈ 0.55 expected for regions with $n_{\rm e} \ll n_{\rm crit}$ assuming Tayal (2011) electron collision

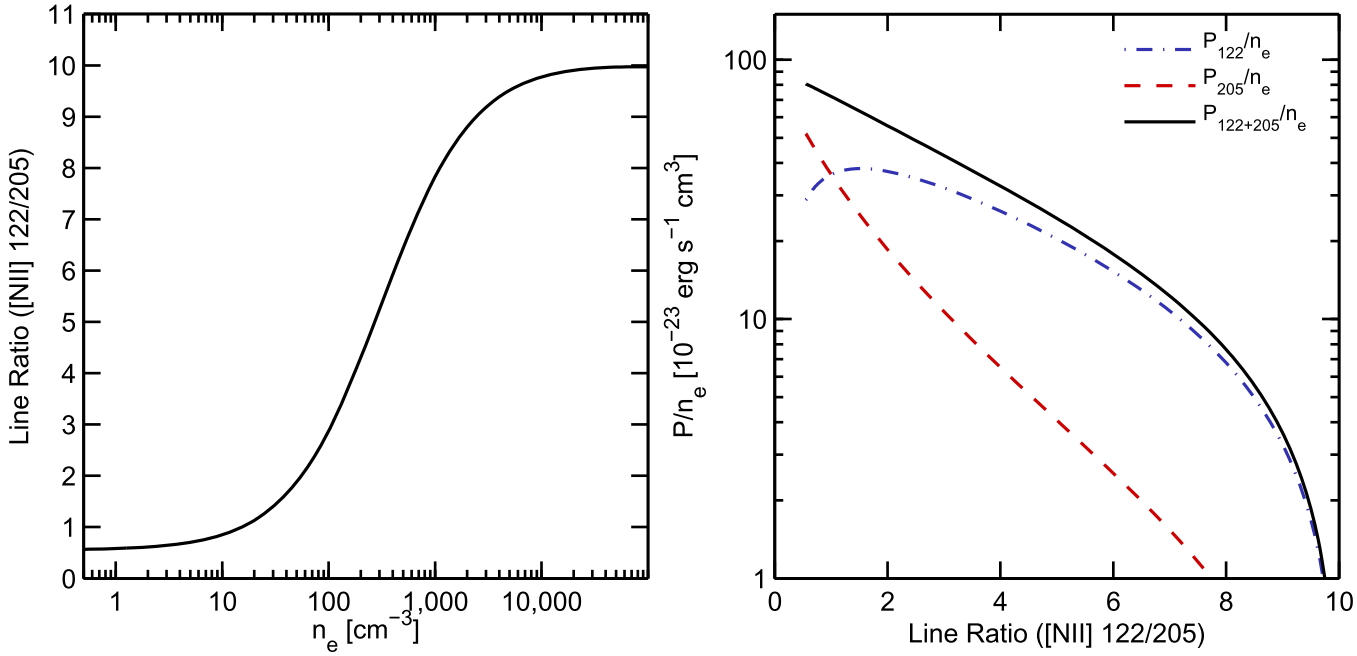

Figure 2. Left: ratio of the [N II] 122 μm and [N II] 205 μm transitions as a function of electron density n_e. The theoretical curve was calculated using Tayal (2011) electron collision strengths and shows how the [N II] 122/205 line ratio can be used as a probe of the electron density of the low-excitation, warm ionized gas in the ~10–1000 cm^{-3} range. We have assumed an electron temperature of $T = 8000$ K. Right: P/n_e, where P is the power radiated per N^+ ion in the [N II] 122 μm transition (blue), the [N II] 205 μm transition (red), and the sum of both [N II] transitions (black), as a function of the [N II] 122/205 line ratio. At [N II] 122/205 line ratios greater than about one, the total power radiated per ion starts to be dominated by the [N II] 122 μm transition.

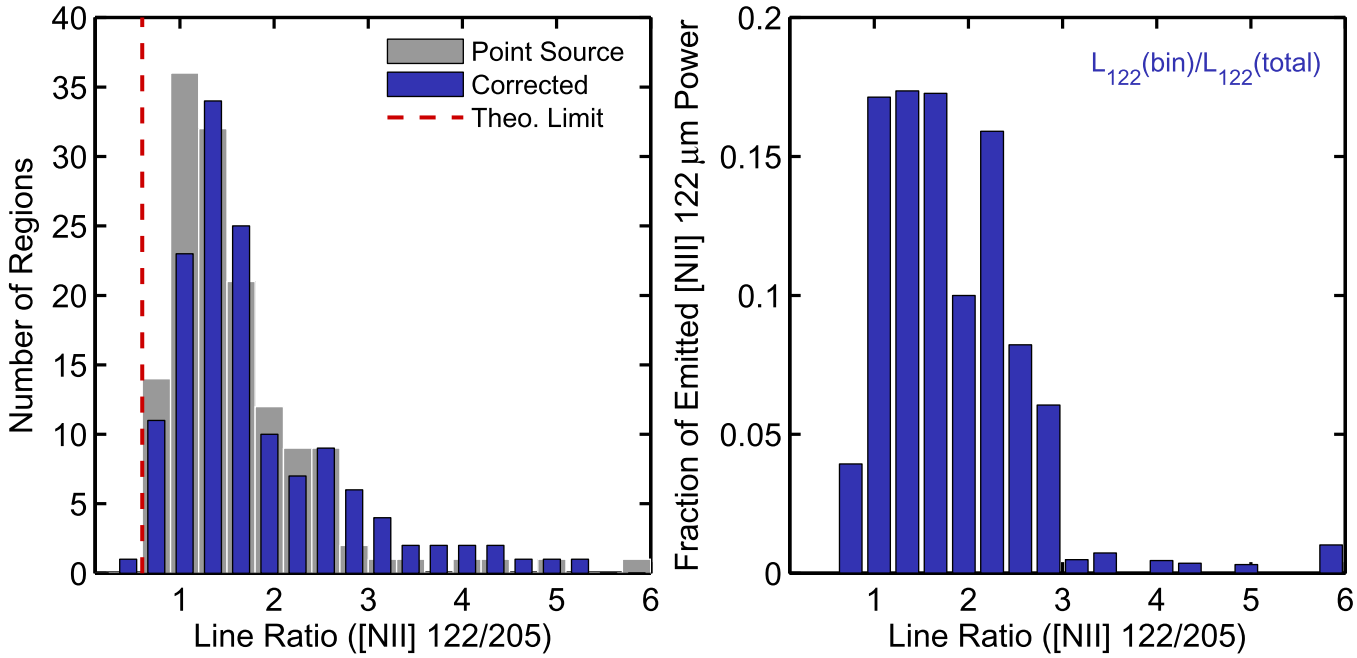

Figure 3. Left: histograms of the [N II] 122/205 line ratio for the 141 regions in our sample when reduced as a point source (gray) and after applying the extended emission correction (blue). Both distributions are roughly similar, with the main effect of the extended emission correction being a small overall increase of the line ratios. The red dashed line shows the theoretical line ratio of ≈0.55 expected for regions of low electron density ($n_e \ll n_{crit}$); in this regime the [N II] 122/205 line ratio is insensitive to the ionized gas density. Most of our regions have line ratios above this limit, which means that their line ratios can be used to measure the electron density of the photoionized gas. Right: fraction of the emitted [N II] 122 μm power per [N II] 122/205 line ratio bin. About 40% of the total [N II] 122 μm power arises from regions with [N II] 122/205 $\gtrsim$ 2 ($n_e \gtrsim 50$ cm^{-3}).

strengths (this ratio limit is 0.66 if we assume Hudson & Bell (2005) electron collision strengths instead). In our sample, there is only one region with a [N II] 122/205 line ratio lower than 0.55. This region is located in NGC 4254 and has a [N II] 122/205 line ratio of 0.38 ± 0.15. As a cautionary note, this region is one of the few where the extended emission correction increased the [N II] 205 μm intensity by a factor of ~2. Therefore, the origin of this low [N II] line ratio may not be physical. About 40% of the emitted [N II] 122 μm power arises from regions with [N II] 122/205 $\gtrsim$ 2, or equivalently, electron

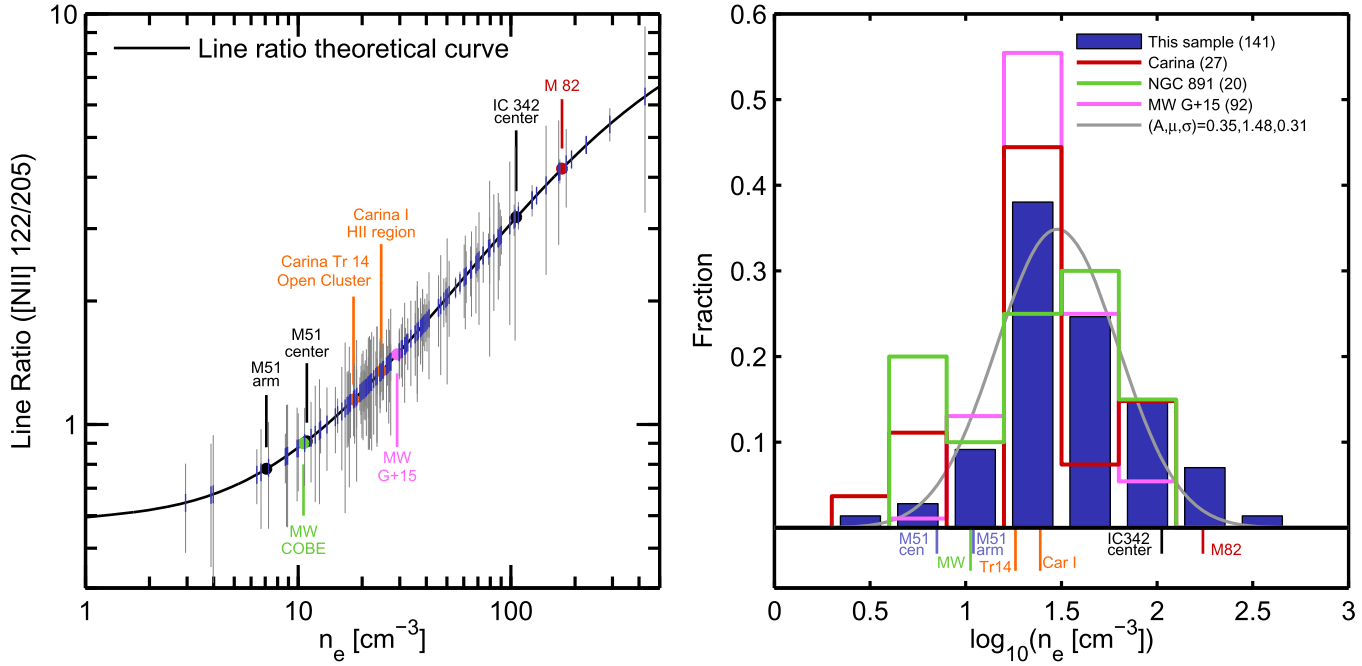

Figure 4. Left: [N II] 122/205 line ratio as a function of electron density (n_e). The blue vertical lines show the observed ratios, and corresponding n_e measurements, for 141 regions selected from 21 galaxies in the BtP sample. The gray vertical lines show the line ratio error. We measure electron densities in the range $n_e \sim 1-300\,\mathrm{cm}^{-3}$. We also include [N II] 122/205 line ratio measurements from the M51 central region and spiral arm (Parkin et al. 2013), the Milky Way (Bennett et al. 1994; Goldsmith et al. 2015), the young open cluster Trumpler 14 and the H II region Carina I in the Carina nebula (Oberst et al. 2011), the IC 342 central region (Rigopoulou et al. 2013), and M82 (Petuchowski et al. 1994). The median electron density in our sample is $n_e \approx 30\,\mathrm{cm}^{-3}$, similar to the ionized gas density of the Carina I H II region. Right: distribution of electron densities for the BtP sample (blue bars), 22 regions in the Carina nebula (red, Oberst et al. 2011), 92 regions in the Milky Way (G+15; Goldsmith et al. 2015), and 20 regions in the edge-on galaxy NGC 891 (Hughes et al. 2014). On the bottom of the plot we also show the individual measurements displayed in the left panel. The gray curve shows a Gaussian fit to the BtP distribution of electron densities, and in the legend we list the amplitude (A), mean electron density (μ), and standard deviation (σ) of the fit.

densities higher than the critical density of the [N II] 205 μm line.

The left-hand panel of Figure 4 shows the theoretical dependence of the electron density on the [N II] 122/205 line ratio calculated in Section 3.1 and shown in the left-hand panel of Figure 2. The observed [N II] 122/205 line ratios measured in our 141 regions from the BtP sample are shown as blue vertical lines on top of the curve. The line ratios range between ~0.6 and 6, which correspond to electron densities in the ~3–300 cm^{-3} range. Typical uncertainties in the electron density measurements are of the order of 20%. Figure 4 also includes [N II] 122/205 line ratios observed in the Milky Way with the Cosmic Background Explorer (Bennett et al. 1994), M82 with the Kuiper Airborne Observatory (Petuchowski et al. 1994), the young open cluster Trumpler 14 and the H II region Carina I in the Carina nebula observed with the South Pole Imaging Fabry–Perot Interferometer at the Antarctic Submillimeter Telescope and Remote Observatory and the *Infrared Space Observatory* (Oberst et al. 2011), the M51 central and arm regions observed with *Herschel* PACS (Parkin et al. 2013), and the central region of IC 342 observed with *Herschel* PACS and SPIRE (Rigopoulou et al. 2013). We measure a mean electron density in the BtP sample of $n_e \approx 30\,\mathrm{cm}^{-3}$, which is similar to the electron density in the young open cluster Trumpler 14, the Carina I H II region, the average value found in the Galactic plane by Goldsmith et al. (2015), and the median value of $22\,\mathrm{cm}^{-3}$ measured in a sample of 12 (U)LIRGs (Zhao et al. 2016).

The right-hand panel of Figure 4 shows the resulting distribution of electron densities for the BtP regions. We also plot the literature measurements included in the left-hand panel, and we add the distributions of electron densities measured in 20 regions of the edge-on galaxy NGC 891 (Hughes et al. 2014), 92 positions in the Galactic plane (Goldsmith et al. 2015),[21] and 27 regions in the Carina nebula (Oberst et al. 2011). In the latter, the highest-density regions are associated with the outskirts of the H II regions Carina I and II, and the lowest-density regions correspond to an extended component detectable all over the ~30 pc map (Oberst et al. 2006, 2011). The comparison between the BtP data and the external samples reveals the wide range of electron densities present in our sample. On one hand, we are sensitive to a more extended, low-density ionized gas component, like the one that fills the medium in between H II regions in the Carina nebula. On the other hand, we have regions with high electron densities (measured in the central regions of NGC 1097, NGC 4536, and NGC 6946) that are comparable to the ones measured in very active star-forming galaxies, like M82 and the central region of IC 342.

3.3. Electron Density Variations within Individual Galaxies

The photoionized gas traced by the [N II] in our sample spans two orders of magnitude in electron density. In this section we explore the dependence between the electron density and a number of ISM properties that might play a role in these variations, such as metallicity, radiation field strength, and star-formation activity.

[21] We only included line-of-sight positions from Table 2 in Goldsmith et al. (2015) that have $\geqslant 3\sigma$ line detections in both [N II] 122 and 205 μm transitions.

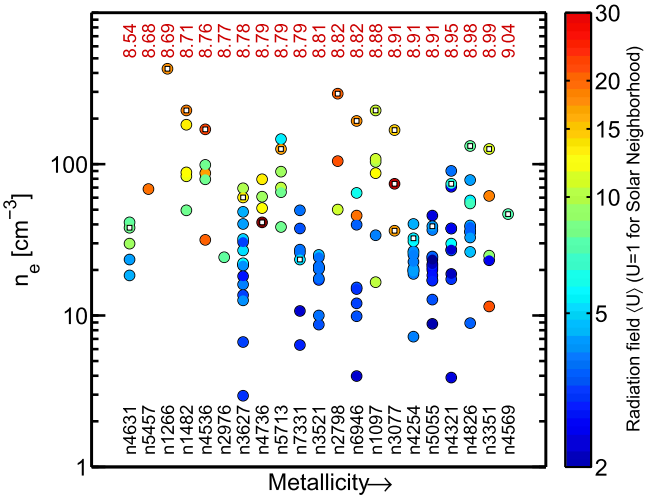

Figure 5. Electron density as a function of metallicity for all regions in our sample sorted by galaxy. The name of the galaxy is listed in the bottom part of the plot, and the characteristic global value of the oxygen abundance $12 + \log(\mathrm{O/H})$—measured by Moustakas et al. (2010)—is listed on the top part of the plot in red. Metallicity increases to the right. The color scale corresponds to the dust-weighted mean starlight intensity $\langle U \rangle$ derived from the Draine & Li (2007) model. The symbols with inner white squares show the regions where the position of the bolometer is located within a deprojected distance of 400 pc to the center of the galaxy. Within galaxies, and despite the limited spatial coverage of the disk, we observe variations in electron density greater than a factor of ∼10 (e.g., NGC 3627, NGC 4826, NGC 6946). For most galaxies, the highest electron density measurements are found in the central regions. Finally, the color scale reveals a clear trend of increasing electron density with radiation field strength.

How much does the electron density vary within the area sampled in each galaxy? To answer this, Figure 5 shows the electron density of our 141 regions grouped by galaxy. The names of the galaxies are listed in the bottom of the panel, and their characteristic metallicities are listed in the top part of the plot. Galaxies are sorted from left to right in order of increasing metallicity. We use color to include information about the local radiation field strength, derived using the dust-weighted mean starlight intensity $\langle U \rangle$ from the Draine & Li (2007) model. Finally, we mark using open circles regions with deprojected distances to the center of the galaxy less than the median physical radius of the SPIRE-FTS bolometer in our sample, that is, ≈400 pc. We measure the distance to the center by calculating the angular separation between the position of the center of the galaxy (taken from the NASA Extragalactic Database) and the position of the SPIRE-FTS bolometers. We then convert the angular separation into a deprojected distance, D_c, using distances drawn from the compiled list in Kennicutt et al. (2011). From Figure 5 we notice that the highest electron density measurements within a galaxy tend to be found in its central region (in 16 of the 18 galaxies with central measurements available, the central region corresponds to the highest or the second highest electron density measured in the disk).

Figure 5 also shows that we are able to detect variations in the electron density within individual galaxies as high as a factor of ∼50. One good example is NGC 3627, a Leo Triplet interacting spiral galaxy with a strong bar (Regan et al. 2002). The highest gas density in the system, $n_e = 71\,\mathrm{cm}^{-3}$, is measured at one of the ends of the bar. This region is characterized by strong star-formation activity and high average radiation field strength ($\langle U \rangle \approx 10$). The second highest ionized gas density measurement comes from the central region of the galaxy ($n_e = 40\,\mathrm{cm}^{-3}$, $\langle U \rangle \approx 13$), and the lowest ionized gas density ($n_e = 4\,\mathrm{cm}^{-3}$) is measured in a more quiescent region ($\langle U \rangle \approx 3$) located in between the bar and one of the spiral arms. This trend of increasing electron density with radiation field strength is not exclusive to NGC 3627. In fact, Figure 5 reveals a similar trend for the rest of the sample: while regions with $n_e \lesssim 20\,\mathrm{cm}^{-3}$ tend to have radiation field strengths of only a few times the radiation field in the solar neighborhood, regions with $n_e \gtrsim 100\,\mathrm{cm}^{-3}$ tend to have $\langle U \rangle \gtrsim 15$. Among nearby galaxies that are not part of the BtP sample, spatial variations of the [N II] 205 μm emission are also observed for M83, NGC 891, M51, and NGC 4038/9 (Wu et al. 2015; Hughes et al. 2016).

There is not a clear trend of varying electron density with oxygen abundance. However, low-metallicity galaxies in our sample tend to have, on average, higher radiation fields and electron densities than the rest of the sample. This could be an observational bias as the spatial coverage of the [N II] line emission in these low-metallicity environments—especially in the case of the [N II] 122 μm transition—is mostly limited to bright, star-forming regions.

3.4. Relationship between Electron Density and the ISM Environment

One of our main goals is to understand the variations in the ionized gas density as a function of the ISM environment. This is possible thanks to the spatial coverage of our target galaxies provided by SPIRE-FTS and the rich characterization of the ISM properties derived from the ancillary data. We start our analysis by studying how the electron gas density changes with radial distance. Panel (a) in Figure 6 shows the electron density of the 141 regions in our sample as a function of the deprojected distance to the center of the galaxy normalized by the radius of the major axis at the $\mu_B = 25\,\mathrm{mag\,arcsec}^{-2}$ isophote (R_{25}; de Vaucouleurs et al. 1991; Moustakas et al. 2010). The resulting 19 regions with deprojected distances to the center less than 400 pc are shown as red open squares. As we already discussed for Figure 5, central regions in galaxies tend to have higher electron densities (median $n_e \approx 77\,\mathrm{cm}^{-3}$) than those located in the disk (median $n_e \approx 25\,\mathrm{cm}^{-3}$).

Panel (b) shows the ionized gas density as a function of the infrared color $\nu f_\nu(70\,\mu\mathrm{m})/\nu f_\nu(100\,\mu\mathrm{m})$ measured using the PACS 70 and 100 μm data. There is a good correlation of increasing gas density with increasing $\nu f_\nu(70\,\mu\mathrm{m})/\nu f_\nu(100\,\mu\mathrm{m})$. The best power-law fit, shown as a solid line in the second panel, yields

$$\log_{10}(n_e/\mathrm{cm}^{-3}) = 3.41 \times \log_{10}(\nu f_\nu(70)/\nu f_\nu(100)) + 1.68. \quad (5)$$

The standard deviation around the fit is 0.42 dex. This parameterization could be useful for studies that require an electron density in order to predict the [N II] 205 μm flux based on the [N II] 122 μm flux (or vice versa) (e.g., Zhao et al. 2013).

Panels (c) and (d) in Figure 6 show the electron density as a function of the dust-weighted mean starlight intensity, $\langle U \rangle$, and the fraction of the dust luminosity produced by photodissociation regions with $U > 100$, f_{PDR} (both parameters derived from the Draine & Li (2007) model). The correlation of electron density with starlight intensity is as good as the correlation with

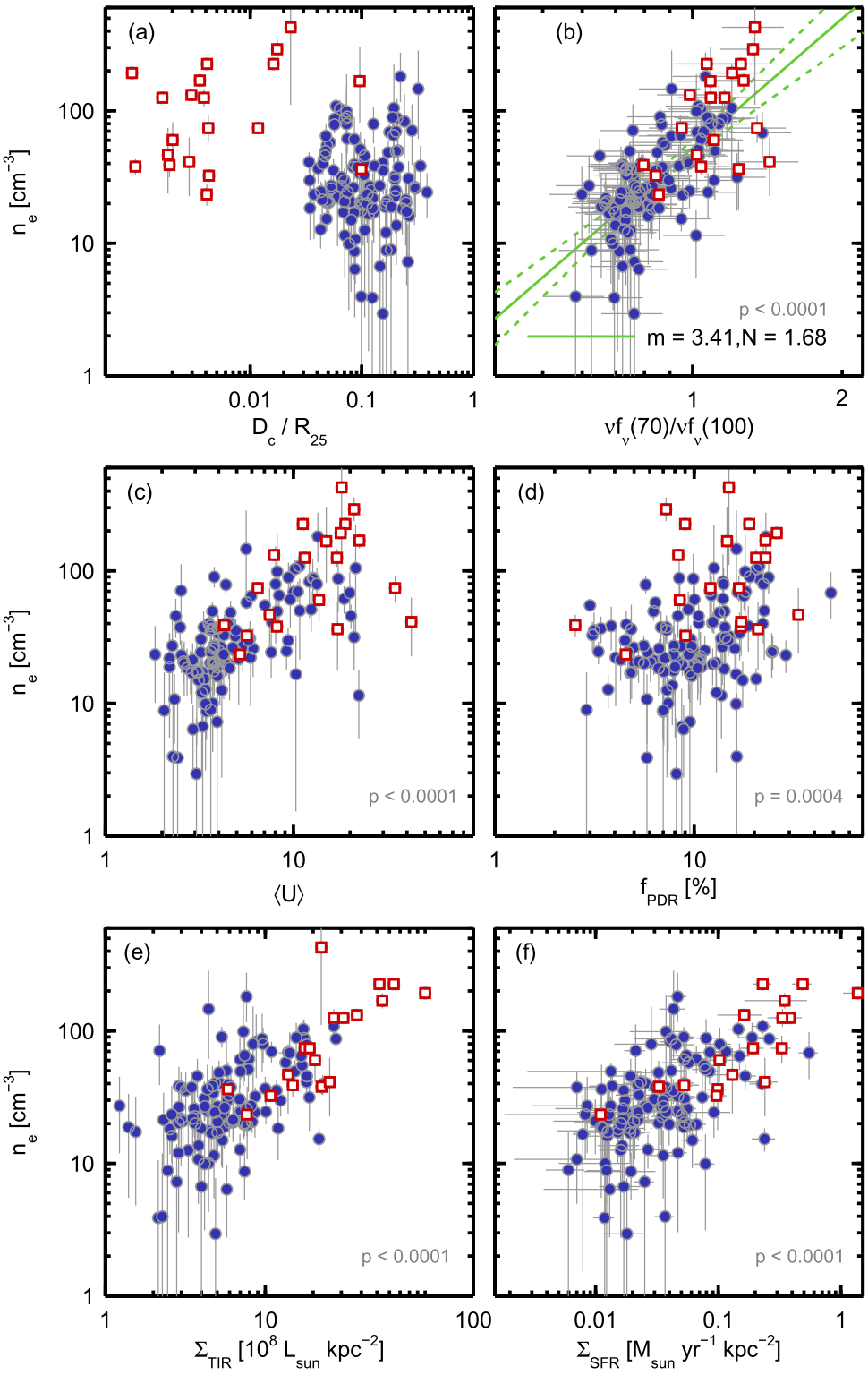

Figure 6. Electron density (n_e) as a function of six parameters. The p values for testing the null hypothesis are shown in the lower right corner of each panel. (a) Galactocentric distance (D_c) normalized to the radius of the major axis at the $\mu_B = 25$ mag arcsec^{-2} isophote (R_{25}; de Vaucouleurs et al. 1991; Moustakas et al. 2010). Central regions with deprojected distances less than 400 pc are shown as open red squares. These regions have an average electron density a factor of ~3 higher than the rest of the regions. (b) Infrared color ($\nu f_\nu(70\ \mu\mathrm{m})/\nu f_\nu(100\ \mu\mathrm{m})$). The correlation is good, with a Spearman correlation coefficient of $r = 0.73$. The solid and dashed green lines show the best power-law fit to the data (Equation (5)) and the associated confidence bands, respectively. The slope (m) and normalization of the fit (N) are listed in the bottom-right corner and in Equation (1). (c) Dust-weighted mean starlight intensity ($\langle U \rangle$) derived from the Draine & Li (2007) model. (d) Fraction of the dust luminosity produced by photodissociation regions with $U > 100$ (f_{PDR}) also derived from the Draine & Li (2007) model. (e) Total infrared luminosity surface density, Σ_{TIR}. (f) Star-formation rate surface density (Σ_{SFR}) measured using a combination of 24 μm and Hα emission following the Calzetti et al. (2007) calibration.

infrared color, which is expected given the good correspondence between infrared color and $\langle U \rangle$ (e.g., see Figure 19 in Muñoz-Mateos et al. 2009). On the other hand, there is no strong dependence between electron density and $f_{\rm PDR}$ (Spearman correlation coefficient $r = 0.38$). Finally, panels (e) and (f) show the correlation between electron density and TIR luminosity surface density, $\Sigma_{\rm TIR}$, and star-formation surface density, $\Sigma_{\rm SFR}$. Similar to what is found for the dependences with infrared color or radiation field strength, there is a clear trend of increasing electron density with increasing infrared surface brightness and star-formation activity.

The observed relationship between electron density and star-formation activity, or radiation field strength, could have at least two origins. The first one is related to the first stages of the evolution of H II regions. For recent episodes of star-formation activity, we expect massive stars to produce very intense radiation fields. The corresponding young H II regions created around these newly formed stars are more compact than evolved H II regions, characterized by electron densities higher than $n_{\rm e} \approx 10^3\,{\rm cm}^{-3}$ and located in the high-pressure, inner regions of molecular clouds (Franco et al. 2000). Although our sensitivity to high electron densities is limited by the critical density of the [N II] 122 μm line, we believe that regions in our sample that exhibit high radiation fields and high electron densities could be related to young, compact H II regions. The second possible explanation is based on a thermal pressure argument. Once a young, compact H II region has expanded and reaches pressure equilibrium with its surrounding medium, a high electron density implies a high neutral density of the cold ISM gas in which the H II region is embedded. This high-density molecular gas environment provides the conditions for further star formation to occur, establishing a link between the high density of the ionized gas and more intense star-formation activity.

4. ESTIMATING SFRs FROM THE [N II] FINE-STRUCTURE TRANSITIONS

In this section we analyze the reliability of the far-infrared [N II] transitions as tracers of star-formation activity. One of the advantages of these lines is that, unlike Hα or other optical tracers, they are insensitive to dust extinction and can provide a robust estimate of the ionizing photon rate, Q_0. We start by deriving a theoretical relation between [N II] emission and SFR. This relation depends, among other things, on the nitrogen abundance, the ionization fraction of nitrogen, and the density of the ionized gas. For the latter we study two cases: (1) low-density gas and (2) gas that follows a log-normal distribution of densities. Finally, we compare our theoretical predictions and the results from the MAPPINGS-III code to the BtP galaxies and other samples of extragalactic objects.

4.1. Low-density Limit

To understand how [N II] emission works as a measure of star formation, we can assume that the excitation is dominated by collisions from the ground level and balanced by radiative deexcitation. This will be correct at densities lower than the critical density of the line, where collisional deexcitation does not play a role. Thus, we can approximate the power radiated in the [N II] 122 or 205 μm lines in a given volume V as

$$L_\lambda \cong n_{\rm e} n({\rm N}^+) q_\lambda h\nu V. \quad (6)$$

Here $q_{122} = q_{02}$ and $q_{205} = q_{01} + q_{02}$, where q_{01} and q_{02} are the collisional excitation coefficients from the ground level to level 1 and 2, respectively. Here, $n({\rm N}^+)$ is the density of the ionized nitrogen, and we assume that most N^+ is in the ground level. For an ionization-bounded H II region, the ionization–recombination balance dictates that

$$Q_0 = n_{\rm e} n({\rm H}^+) \alpha_B V, \quad (7)$$

where the total rate of H photoionizations, Q_0, is equal to the rate of radiative recombinations determined by the case B recombination coefficient $\alpha_B = 3.04 \times 10^{-13}\,{\rm cm}^3\,{\rm s}^{-1}$ at $T = 8000$ K, and $n({\rm H}^+)$ is the number density of ionized hydrogen atoms. Under these hypotheses, and combining Equations (6) and (7), the ionizing photon rate is proportional to the [N II] luminosity through (see Equation (15) in McKee & Williams 1997)

$$Q_0 \cong \frac{L_\lambda \alpha_B}{q_\lambda h\nu_\lambda} \frac{n({\rm H}^+)}{n({\rm N}^+)}. \quad (8)$$

Given the similarities in the ionization potentials (13.6 eV versus 14.5 eV), and assuming that the nitrogen is only singly ionized ($N^+/N = 1$), with a negligible fraction of higher ionization states (which require photons more energetic than 29.6 eV), the last factor is equal to the inverse of the gas-phase abundance of nitrogen.

The nitrogen ionization balance depends on the spectrum of the stellar radiation and the ionization parameter $U_{\rm ion}$, which is defined as the ratio of the ionizing photon density to the hydrogen density $n_{\rm H}$. Because the $N^+ \rightarrow N^{++}$ ionization potential is above that for He $\rightarrow$ He^+, N^{++} and N^{+++} will be present only where the He is ionized. Only the hottest O stars (earlier than O8) can ionize He throughout the H II region. If the He is ionized, the nitrogen will be mainly N^{++} and N^{+++} only if the local ionization parameter $U_{\rm ion} > 10^{-3.1}$ (see Figure 8 of Abel et al. 2009). The median $U_{\rm ion}$ in a H II region is $>10^{-3}$ for $n_{\rm e} Q_0 > 10^{50}\,{\rm cm}^{-3}\,{\rm s}^{-1}$ (see Figure 3 of Draine 2011). Thus in very high density H II regions, or giant H II regions ionized by a cluster of O stars, the nitrogen may be preferentially in N^{++}, but in low-density H II regions around single stars we expect N to be primarily N^+.

Assuming solar abundance $({\rm N/H})_\odot = 7.4 \times 10^{-5}$ (Asplund et al. 2009) and $q_{205} = q_{01} + q_{02} = 6.79 \times 10^{-8}\,{\rm cm}^3\,{\rm s}^{-1}$ (Hudson & Bell 2005), we measure a median [N II] 205 μm–based global ionizing photon rate for the BtP galaxies of $Q_0 = 1.98 \times 10^{52}$ photons s^{-1}. Normalized to the covered area, this corresponds to 1.96×10^{51} photons s^{-1} kpc^{-2}. If we use the collisional excitation coefficients from Tayal (2011) instead, then $q_{01} + q_{02} = 5.1 \times 10^{-8}\,{\rm cm}^3\,{\rm s}^{-1}$, which increases the ionizing photon rates by a factor of 1.3. The median ionizing photon rate surface density in our sample is about three times the ionizing photon rate measured by Bennett et al. (1994) inside the solar circle in our Galaxy. Using the [N II] 122 μm transition—in principle a better tracer than [N II] 205 μm because of its higher critical density—yields an average ionizing photon rate surface density a factor of ~4 higher than the one based on the [N II] 205 μm emission.

To relate the ionizing photon rate Q_0 to the SFR, we use the fact that for the default Starburst99 IMF with an upper-mass cutoff of 120 $M_\odot$ (see Section 2.4 for details) and steady star formation for 10^8 years, the SFR and the rate of production

of photoionizing photons are related by

$$\frac{Q_0}{f_{\rm ion}} = 1.60 \times 10^{53}\ {\rm s}^{-1} \frac{\rm SFR}{M_\odot\ {\rm yr}^{-1}}, \quad (9)$$

where $f_{\rm ion}$ is the fraction of H-ionizing photons emitted by stars that photoionize H or He; thus, $(1 - f_{\rm ion})$ is the fraction absorbed by dust. According to the discussion of dusty H II regions by Draine (2011), we expect $f_{\rm ion} \approx 1$. Also note that if we change the IMF upper-mass cutoff to 100 $M_\odot$ (e.g., Murphy et al. 2011), the rate of ionizing photons per SFR decreases by ∼14%.

Combining Equations (8) and (9), we find that the SFR as a function of the [N II] luminosity in the low-density limit is given by

$$\frac{\rm SFR}{M_\odot\ {\rm yr}^{-1}} = 1.49 \times 10^{-7} \left(\frac{6.79 \times 10^{-8}\ {\rm cm^3\ s^{-1}}}{q_{01} + q_{02}}\right) \times \left(\frac{({\rm N/H})_\odot}{{\rm N^+/H^+}}\right) \frac{L_{205}}{L_\odot}, \quad (10)$$

and

$$\frac{\rm SFR}{M_\odot\ {\rm yr}^{-1}} = 2.35 \times 10^{-7} \left(\frac{2.57 \times 10^{-8}\ {\rm cm^3\ s^{-1}}}{q_{02}}\right) \times \left(\frac{({\rm N/H})_\odot}{{\rm N^+/H^+}}\right) \frac{L_{122}}{L_\odot}. \quad (11)$$

We can see through this example that a measurement of SFR using the fine-structure lines of [N II] is possible, but it will depend on the abundance of nitrogen, its ionization state, and ultimately the density of the ionized region, as collisional deexcitation will be important at densities of interest.

4.2. Effect of a Distribution of Densities

The photoionized gas in a galaxy will generally have a wide range of electron densities, from compact H II regions to diffuse photoionized gas. The balance between photoionization and radiative recombination can then be expressed as

$$Q_0 = \int \alpha_B n({\rm H^+}) n_{\rm e} dV = \int \alpha_B n({\rm H^+}) n_{\rm e} \frac{dV}{d\ln n_{\rm e}} d\ln n_{\rm e}. \quad (12)$$

In order to assess the effect on Q_0 of having a range of electron densities, we parameterize the distribution of electron densities using a log-normal distribution:

$$\alpha_B n({\rm H^+}) n_{\rm e} \frac{dV}{d\ln n_{\rm e}} = \frac{Q_0}{\sqrt{2\pi\sigma^2}} \exp\left[-\frac{(\ln(n_{\rm e}/n_{\rm e0}))^2}{2\sigma^2}\right]; \quad (13)$$

$n_{\rm e0}$ is then a characteristic electron density for the recombining gas, while σ represents the width of the distribution of electron densities. The case $\sigma = 0$ corresponds to uniform density. For $\sigma = 1$, for example, if the characteristic electron density is $n_{\rm e0} = 100\ {\rm cm^{-3}}$, then the 1σ (68%) and 2σ (95.5%) confidence intervals encompass the density ranges $n_{\rm e} = 38.8$–$271.8\ {\rm cm^{-3}}$ and $n_{\rm e} = 13.5$–$738.9\ {\rm cm^{-3}}$, respectively. Log-normal distributions have been used to characterize the electron density distribution of the warm ionized medium (Berkhuijsen & Fletcher 2008; Hill et al. 2008; Redfield & Falcon 2008).

Then, if we replace dV in Equation (2) using Equation (13), we can express the power radiated in a line as

$$L_\lambda = \frac{Q_0}{\alpha_B \sqrt{2\pi\sigma^2}} \left[\frac{\rm N^+}{\rm H^+}\right] \int \exp\left[-\frac{(\ln(n_{\rm e}/n_{\rm e0}))^2}{2\sigma^2}\right] \times \frac{P_\lambda(n_{\rm e})}{n_{\rm e}} d\ln n_{\rm e}. \quad (14)$$

The observed line ratio is then a function of both $n_{\rm e0}$ and σ:

$$\frac{L_{122}}{L_{205}} = \frac{\int d\ln n_{\rm e} \exp[-(\ln(n_{\rm e}/n_{\rm e0}))^2/2\sigma^2] P_{122}(n_{\rm e})/n_{\rm e}}{\int d\ln n_{\rm e} \exp[-(\ln(n_{\rm e}/n_{\rm e0}))^2/2\sigma^2] P_{205}(n_{\rm e})/n_{\rm e}}, \quad (15)$$

and the radiative recombination rate Q_0 can be expressed as

$$Q_0 = C \left(\frac{({\rm N/H})_\odot}{\rm N^+/H^+}\right) [L_{205} + L_{122}], \quad (16)$$

where $\rm N^+/H^+$ is the ionized gas-phase abundance ratio and

$$C(n_{\rm e0}, \sigma) = \frac{\alpha_B}{(N/H)_\odot} \times \frac{\sqrt{2\pi}\sigma}{\int d\ln n_{\rm e} (P_{205}(n_{\rm e}) + P_{122}(n_{\rm e})) \exp[-(\ln(n_{\rm e}/n_{\rm e0}))^2/2\sigma^2]/n_{\rm e}}. \quad (17)$$

Here we introduce the calibration coefficient C, which is the number of ionizing photons per erg of emitted energy in the [N II] lines; C is a function of $n_{\rm e0}$ and the distribution parameter σ, but it can also be regarded as a function of the observed line ratio L_{122}/L_{205} and σ, $C(L_{122}/L_{205}, \sigma)$. The calculations assume a solar abundance $({\rm N/H})_\odot = 7.4 \times 10^{-5}$ (Asplund et al. 2009).

Thus,

$$\frac{\rm SFR}{M_\odot\ {\rm yr}^{-1}} = \frac{2.77 \times 10^{-7}}{f_{\rm ion}} \left(\frac{C(L_{122}/L_{205}, \sigma)}{10^{13}\ {\rm erg^{-1}}}\right) \times \left(\frac{({\rm N/H})_\odot}{\rm N^+/H^+}\right) \frac{L_{122} + L_{205}}{L_\odot}. \quad (18)$$

In summary, we expect that a [N II]-based SFR calibration will depend on the nitrogen abundance and the calibration coefficient C (which in turn is a function of the [N II] 122/205 line ratio, or $n_{\rm e}$, and the width of the distribution of electron densities). In addition, and similar to what we discussed for the low-density limit case, this calibration will underestimate the SFR when the dominant ionization stage is not $\rm N^+$, which is the case for gas ionized by very-early-type O stars in high-density H II regions.

Figure 7 shows the behavior of C as a function of the [N II] 122/205 line ratio and σ. The solid and dashed lines represent the predictions based on the Tayal (2011) and Hudson & Bell (2005) collision coefficients, respectively. The first thing we notice is that, for a fixed value of σ, C increases as a function of the [N II] 122/205 line ratio (or electron density). This is the direct effect of the collisional suppression of the [N II] emission at electron densities near and above the critical density of the transition. In this regime, [N II] collisional deexcitations compete with the radiative decays, and the [N II] intensity starts to systematically underestimate the amount of star-

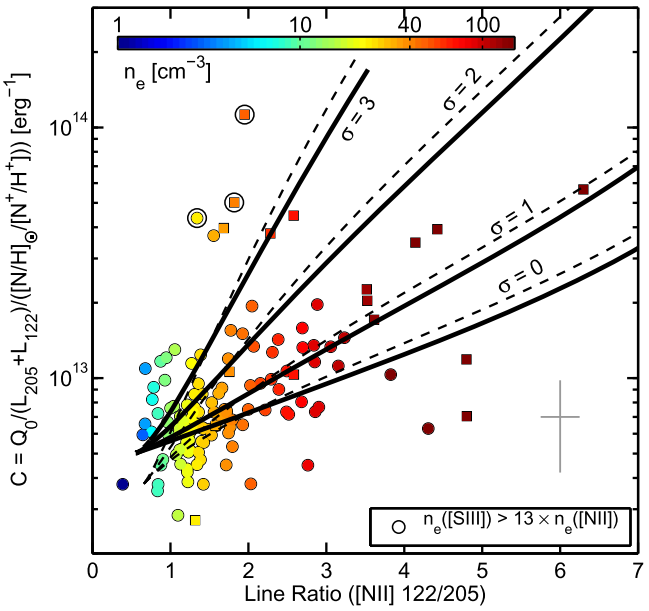

Figure 7. Number of ionizing photons per erg of emitted energy in the [N II] lines, C, as a function of the [N II] 122/205 line ratio, for four values of the electron density distribution parameter: $\sigma = 0$ (uniform density), 1, 2, and 3. Central regions with deprojected distances less than 400 pc are shown as squares. The error bars in the bottom corner show the typical uncertainty on the measurements. The solid and dashed lines are based on the Tayal (2011) and Hudson & Bell (2005) collision coefficients, respectively. As the [N II] 122/205 line ratio increases, the parameter C becomes increasingly sensitive to the distribution of electron densities. This behavior has a direct effect on the accuracy of the determination of SFRs based on the [N II] lines, as SFR $\propto C \times L_{122+205}$ (see Equation (18)). We also include the measured calibration coefficient C for 141 regions in our sample for which we have [N II] 122/205 line ratios available. For each region, we use the characteristic oxygen abundance of its parent galaxy as a proxy for the nitrogen abundance. Finally, we use open circles to indicate three regions that show high C values and have [S III]-based electron density measurements that are a factor of ~13 or higher than those based on the [N II] lines. This could be an indication that these regions have wide electron density distributions.

formation activity. In practical terms, this means that for two regions with the same SFR, similar electron density distributions, but different [N II] 122/205 line ratios, the one with the higher line ratio (or higher n_e) will have a lower $L_{122+205}$ luminosity. This is especially true for cases when the electron density is higher than the critical density of the [N II] 205 μm line, $n_e \gtrsim 44\,\mathrm{cm^{-3}}$ ([N II] 122/205 $\gtrsim$ 1.6).

The second thing to note in Figure 7 is that the calibration coefficient C becomes increasingly sensitive to the distribution of electron densities σ. For example, for an observed line ratio [N II] 122/205 = 4, the value of C increases by a factor ~5 as σ varies from 0 to 2. This implies that in galaxies with $L_{122}/L_{205} \gtrsim 2$, the inferred SFR will be uncertain unless there is additional information available (e.g., from observations of other emission line ratios) to constrain the actual distribution of electron densities.

Finally, Figure 7 also includes the calibration coefficient C measured in regions with [N II] 122 and 205 μm both measured and Q_0 inferred from $\Sigma_{\mathrm{SFR}}(\mathrm{H}\alpha + 24\,\mu\mathrm{m})$ using Equation (9). For the nitrogen abundance of the gas relative to the Sun, $(\mathrm{N^+/H^+})/(\mathrm{N/H})_\odot$, we used as a proxy the oxygen abundance of its parent galaxy, and we assume that nitrogen and oxygen abundances scale linearly. This assumption is consistent with the observed scatter in the (N/O)–(O/H) correlation (e.g., Groves et al. 2004; Pérez-Montero & Contini 2009) in the metallicity range of the BtP galaxies ($12 + \log_{10}(\mathrm{O/H}) \sim 8.6$–9). If we assume instead of the linear scaling an analytic function dependence of the nitrogen abundance with oxygen, like the one used in the MAPPINGS code, then we observe a larger spread in the C–[N II] 122/205 line ratio values of our BtP regions.

In general, the calibration coefficient C predictions are consistent with the observations, and as the [N II] 122/205 line ratio increases, the scatter in the observations can be explained by different assumptions on the width of the electron density distribution. A handful of exceptions are the group of seven regions with [N II] 122/205 line ratios around ~1.5–2.5 that show significantly higher C values compared to the theoretical expectations, even for the $\sigma = 2$ case. To explore if the reason for the high calibration coefficients measured in these regions is associated with high σ values, we add the [S III] lines to our analysis. Since sulfur has a second ionization potential (23.3 eV) higher than that of N II, the sulfur forbidden lines [S III] 18.7 and 33.5 μm probe a higher-ionization gas than the [N II] infrared lines. [S III] 18.7/33.5 is sensitive to changes in the electron density in the $n_e \sim 100$–$10^4\,\mathrm{cm^{-3}}$ range. For three of the seven regions, fluxes for the [S III] 18.7 and 33.5 μm lines are available (Dale et al. 2009b) using the infrared spectrograph (Houck et al. 2004) on board *Spitzer*. The size of the aperture used to measure the [S III] line fluxes is $23'' \times 15''$, roughly similar to the ~17″ SPIRE-FTS beam at 205 μm. We find that the [S III]-based electron densities of these regions are at least a factor of ~13 higher than those obtained using the [N II] lines. This suggests that these regions could have a wide distribution of electron densities, where a higher-ionization, higher-density gas component powered by massive stars coexists with the more diffuse gas traced by the [N II] lines. A complete analysis of the distribution of electron densities based on the combination of multiple tracers of ionized gas density (e.g., [N II], [S III], [O III]) will be presented in a future paper.

4.3. *Correlations between the [N II] 122 and* 205 μm *Transitions and the Star-formation Activity*

In this section, we continue the study of the relationship between [N II] emission and star-formation activity, but this time we also include the individual correlations with the [N II] 122 and 205 μm line surface brightnesses (Σ_{122} and Σ_{205}, respectively) because for many sources only one of these two lines will be available.

The first panel in Figure 8 shows the correlation between $\Sigma_{\mathrm{SFR}}(\mathrm{H}\alpha + 24\,\mu\mathrm{m})$ and $\Sigma_{122+205}$ scaled by the nitrogen abundance factor $(\mathrm{N/H})_\odot/(\mathrm{N/H})$. The best linear fit yields

$$\frac{\Sigma_{\mathrm{SFR}}}{M_\odot\,\mathrm{yr^{-1}\,kpc^{-2}}} = 3.31 \times 10^{-7}\left(\frac{(\mathrm{N/H})_\odot}{\mathrm{N^+/H^+}}\right)\frac{\Sigma_{122+205}}{L_\odot\,\mathrm{kpc^{-2}}}. \quad (19)$$

Based on this fit, the right panel shows the scatter as a function of IR color. We also plot the relation from Equation (18) for three cases: two uniform-density cases ($\sigma = 0$) with electron densities of $n_e = 10$ and $100\,\mathrm{cm^{-3}}$, and one case with a wider electron density distribution ($\sigma = 2$) and $n_{e0} = 100\,\mathrm{cm^{-3}}$. For the nitrogen abundance term in Equation (18), we use as a proxy the median oxygen abundance of the sample ($12 + \log_{10}(\mathrm{O/H}) \approx 8.83$). We find that the best linear fit to the data lies between the expectations from the $n_e = 10$ and

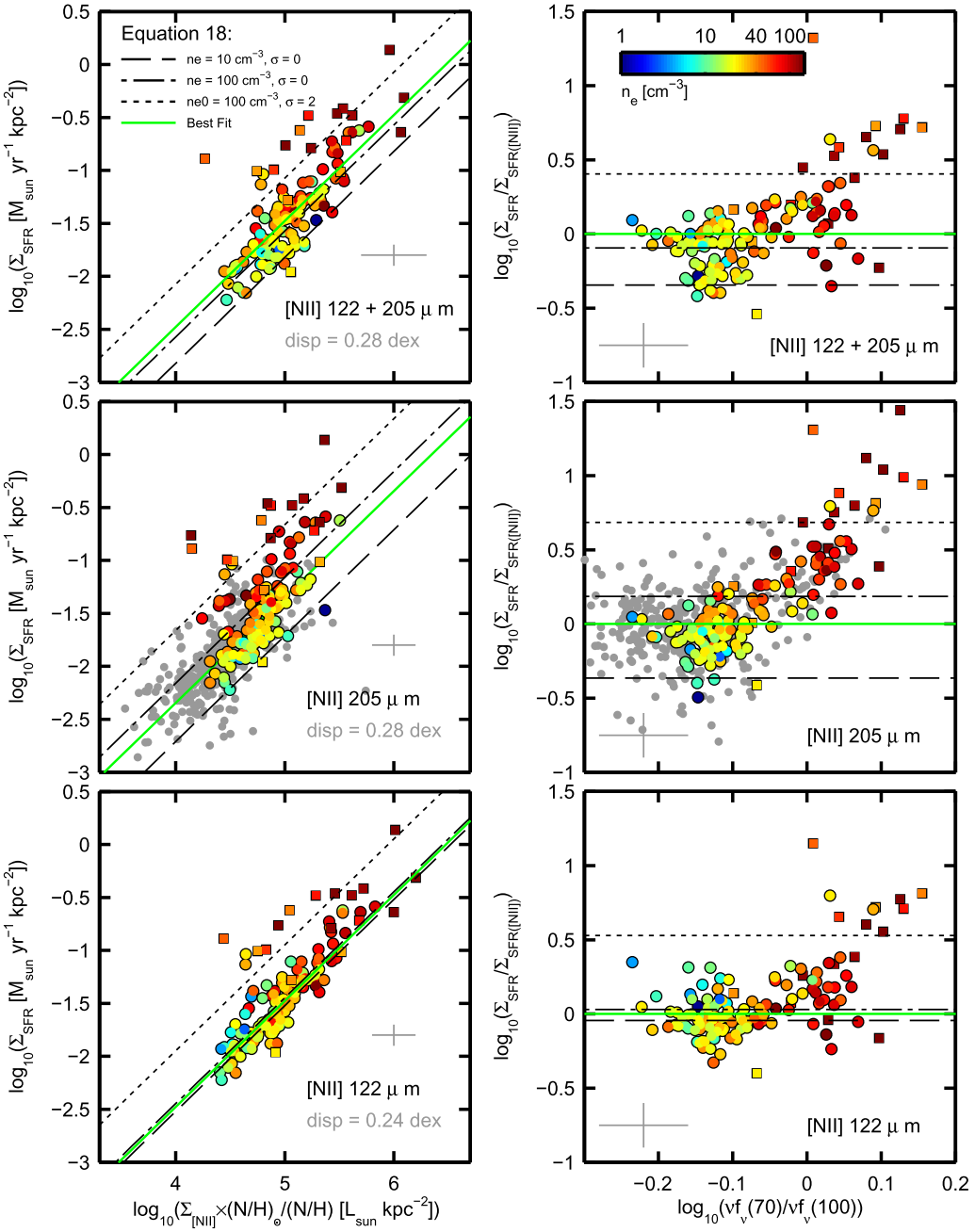

Figure 8. Left panels: star-formation rate surface density ($\Sigma_{\rm SFR}$(Hα + 24 μm)) versus the combined ($\Sigma_{122+205}$) and individual (Σ_{122} and Σ_{205}) [N II] line surface brightness scaled by the nitrogen abundance factor $(N/H)_\odot/(N/H)$. Each point represents a 17″ region selected from the 21 BtP galaxies. The error bars in the bottom corner show the typical uncertainty on the measurements. For regions with [N II] 122/205 line ratios available, the color represents the electron density. In the case of the [N II] 205 μm line, the gray points correspond to 366 additional regions that lie outside the KINGFISH/PACS coverage and therefore lack [N II] 122 μm observations. We also show regions with deprojected distances to the center smaller than 400 pc as squares. The green solid line corresponds to the best fit through the data for a fixed slope of one. The rest of the lines correspond to the results from Equation (18) for different assumptions on the electron density distribution parameters $n_{\rm e}$ and σ. Right panels: ratio between $\Sigma_{\rm SFR}$ measured using Hα+24 μm and the [N II] lines (based on the best linear fit) as a function of infrared color and electron density. We also include the predictions from Equation (18) shown in the left panels. We observe a systematic increase of the $\Sigma_{\rm SFR}/\Sigma_{\rm SFR}$([N II]) ratio as a function of infrared color and electron density. As predicted by Equation (18), these deviations could be associated with a higher density distribution parameter σ or to electron densities higher than the critical density of the [N II] lines. We observe the largest deviations from the linear fit for the [N II] 205 μm line, which is expected given that the critical density of this line is about six times lower than the critical density of the [N II] 122 μm transition.

$n_{\rm e} = 100\,{\rm cm}^{-3}$ single density ($\sigma = 0$) models (long-dashed and dot-dashed lines). We also observe that the $\Sigma_{\rm SFR}/\Sigma_{122+205}$ ratio tends to increase as a function of infrared color and electron density. As we discussed in Section 4.2, these deviations can be understood in terms of the electron density of the gas relative to the critical density of the [N II] transitions and the density distribution parameter σ. For example, from Equation (18) we expect regions with a density distribution parameter $\sigma = 2$ and $n_{\rm e0} = 100\,{\rm cm}^{-3}$ (short-dashed line) to have $\Sigma_{\rm SFR}/\Sigma_{122+205}$ ratios a factor of ∼5 higher than the ratio found by the best linear fit. In our sample, there are two galaxy central regions with densities around $n_{\rm e} \approx 100\,{\rm cm}^{-3}$ that have $\Sigma_{\rm SFR}/\Sigma_{122+205}$

ratios that are consistent with the $\sigma = 2$, $n_{e0} = 100\,\mathrm{cm}^{-3}$ model.

In the case of the [N II] 205 μm emission, we include in our analysis 366 additional regions that lie outside the KINGFISH/PACS coverage (meaning, they lack [N II] 122 μm observations; see middle row of Figure 8). The best linear fit through the Σ_{205}–Σ_{SFR} correlation yields

$$\frac{\Sigma_{\mathrm{SFR}}}{M_\odot\,\mathrm{yr}^{-1}\,\mathrm{kpc}^{-2}} = 4.51 \times 10^{-7}\left(\frac{(\mathrm{N/H})_\odot}{\mathrm{N^+/H^+}}\right)\frac{\Sigma_{205}}{L_\odot\,\mathrm{kpc}^{-2}}. \quad (20)$$

The scatter around this fit is 0.28 dex, similar to the scatter in the $\Sigma_{122+205}$–Σ_{SFR} correlation. We also observe a larger spread in the results from Equation (18) for the same set of assumptions on n_e and σ as in the case of the combined $\Sigma_{122+205}$ emission. For regions with infrared colors cooler than $\nu f_\nu\,(70\,\mu\mathrm{m})/\nu f_\nu\,(100\,\mu\mathrm{m}) \approx 0.9$, the scatter cloud around the linear fit is roughly symmetric, with a standard deviation of 0.25 dex. At about the same infrared color threshold, Herrera-Camus et al. (2015) find a systematic increase of the fit residuals from the $\Sigma_{[\mathrm{C\,II}]}$–$\Sigma_{\mathrm{SFR}}$ correlation, and Croxall et al. (2012) find a drop in the [C II]-to-FIR ratio for regions in NGC 4559 and NGC 1097 (although they do not find any signs of a "[N II] deficit"). For IR colors warmer than $\nu f_\nu\,(70\,\mu\mathrm{m})/\nu f_\nu\,(100\,\mu\mathrm{m}) \approx 0.9$, which, according to Equation (5), corresponds to an electron density of $n_e \approx 33\,\mathrm{cm}^{-3}$, close to the critical density of the line, we observe a strong increase in the $\Sigma_{\mathrm{SFR}}/\Sigma_{205}$ ratio as a function of infrared color and electron density. These deviations are mainly driven by the collisional quenching of the [N II] 205 μm line due to its relatively low critical density.

Finally, in the case of the Σ_{122}–Σ_{SFR} correlation, shown in the bottom two panels of Figure 8, the best fit through the data using a fixed slope of one yields

$$\frac{\Sigma_{\mathrm{SFR}}}{M_\odot\,\mathrm{yr}^{-1}\,\mathrm{kpc}^{-2}} = 3.33 \times 10^{-7}\left(\frac{(\mathrm{N/H})_\odot}{\mathrm{N^+/H^+}}\right)\frac{\Sigma_{122}}{L_\odot\,\mathrm{kpc}^{-2}}. \quad (21)$$

This linear fit is similar to the relation from Equation (18) for both single density, $n_e = 10$ and $100\,\mathrm{cm}^{-3}$ models. The scatter around the fit is 0.24 dex, slightly better than the 0.28 dex we measure in the Σ_{205}–Σ_{SFR} correlation. Compared to the [N II] 205 μm case, regions start to deviate from the best linear fit at warmer IR colors, and there seems to be a smaller dependence between the amplitude of these deviations and the electron density of the region. This is expected as the critical density of the [N II] 122 μm transition is about six times higher than that of the [N II] 205 μm line. However, and based on the relatively low critical densities of some of the regions that deviate $\gtrsim$0.5 dex compared to the [N II] 122 μm critical density, it seems that the density effect by itself is not sufficient to explain these deviations. As we discussed in Section 4.2, additional physical effects that could be playing a role in these warm regions are the hardness of the radiation field (which sets the $\mathrm{N^{++}/N^+}$ ratio) and the width of the electron density distribution.

The [C II] 158 μm transition is another far-infrared line proposed to study the star-formation activity in local and high-z galaxies (e.g., Herrera-Camus et al. 2015). The scatter in the $\Sigma_{[\mathrm{C\,II}]}$–$\Sigma_{\mathrm{SFR}}$ correlation is about ~0.2–0.3 dex (De Looze et al. 2014; Herrera-Camus et al. 2015), similar to the scatter measured in the $\Sigma_{[\mathrm{N\,II}]}$–$\Sigma_{\mathrm{SFR}}$ correlations that include the [N II] 122 μm transition. The key physical advantage of the [C II] transition is that it is the dominant coolant of the neutral atomic and molecular phases (e.g., Rosenberg et al. 2015), so, unlike the [N II], its intensity reflects the heating of the star-forming gas. As long as the majority of the [C II] emission arises from neutral atomic and molecular gas, and wherever heating of these phases is dominated by star-formation activity, the [C II] intensity provides a direct measure of that activity modulo an uncertain heating efficiency and the cooling contribution from other potentially important coolants such as [O I] 63 μm emission.

4.4. Comparison with Models and Other Extragalactic [N II] Samples

In this section we continue the study of the relation between [N II] emission, star-formation activity, and electron density by complementing our sample of nearby spirals with local LIRGs and comparing these observations to predictions from Equation (18) and the photoionization code MAPPINGS-III (Levesque et al. 2010). A brief description of the LIRG sample and the code MAPPINGS-III can be found in Section 2.

The first panel in Figure 9 shows the L_{205}–SFR correlation for the BtP galaxies and local LIRGs drawn from the GOALS (Zhao et al. 2013) sample. The luminosities and SFRs for the BtP galaxies are the result of the sum of the individual regions shown in Figure 8; the colors of the circles indicate the average electron density of the galaxy. We observe that the average electron density of BtP galaxies ranges between $n_e = 15$ and $100\,\mathrm{cm}^{-3}$, and those systems with electron densities higher than the critical density of the line tend to have higher SFR/L_{205} ratios. This result is similar to what we find in the analysis of the spatially resolved Σ_{205}–Σ_{SFR} correlation.

In addition to the observations, Figure 9 includes results from Equation (18) and the MAPPINGS-III code. For the latter, the shaded color areas represent the model results for different assumptions on the electron density (blue for $n_e = 10\,\mathrm{cm}^{-3}$ and red for $n_e = 100\,\mathrm{cm}^{-3}$) and metallicity of the gas (lower and upper boundaries for $Z = 2Z_\odot$ and $Z = Z_\odot$, respectively). The MAPPINGS-III code predicts that, for a fixed metallicity, H II regions with electron densities of $n_e = 100\,\mathrm{cm}^{-3}$ will have SFR/L_{205} ratios a factor of ~4 higher than those with $n_e = 10\,\mathrm{cm}^{-3}$. These results are consistent with the observed L_{205}–SFR relationship for the BtP galaxies. As we discussed in Section 3.5, one of the reasons for this behavior is the collisional quenching of the [N II] 205 μm line when $n_e \gtrsim n_{\mathrm{crit}}$.

Regarding the GOALS galaxies, about half of them have SFR/L_{205} ratios consistent with the MAPPINGS-III results for H II regions with $n_e = 100\,\mathrm{cm}^{-3}$. The other half have SFR/L_{205} ratios too high to be interpreted by the MAPPINGS-III model outputs. These systems also tend to have high IRAS $f_\nu(60)/f_\nu(100)$ colors (Zhao et al. 2016). One possibility is that the ionized gas for these cases is denser than $n_e = 100\,\mathrm{cm}^{-3}$. We explored this scenario using Equation (18), and we found that, under the assumption of isodensity gas ($\sigma = 0$), an electron density of $800\,\mathrm{cm}^{-3}$ is required to reproduce the high SFR/L_{205} ratios (dot-dashed line). If we drop the assumption of single density gas, then the high SFR/L_{205} ratios can be described by assuming a characteristic electron density of $n_{e0} = 100\,\mathrm{cm}^{-3}$ and increasing the density distribution parameter from $\sigma = 0$ to $\sigma = 2$. In addition to the density effect,

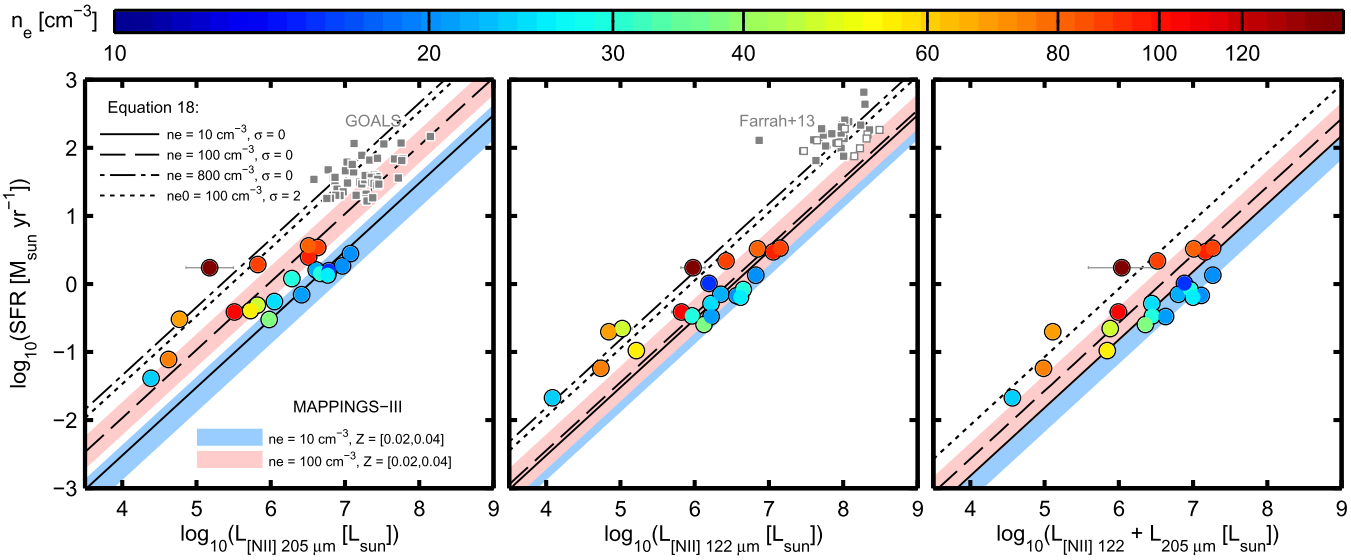

Figure 9. [N II] 122 and 205 μm luminosities versus SFR compared to the results from the MAPPINGS-III code and Equation (18). BtP galaxies are shown as circles, where the color represents the electron density. In general, we find a good agreement between the observed correlations and the model predictions, where the scatter of the correlation can be understood in terms of variations in properties of the ionized gas (n_e and σ) and metallicity. Left: SFR versus L_{205}. For comparison, we include LIRGs from the GOALS sample observed in [N II] 205 μm emission using *Herschel*/SPIRE-FTS (Zhao et al. 2013). The colored areas show the MAPPINGS-III results based on assuming H II regions with electron densities of $n_e = 10$ (blue) and 100 cm^{-3} (red) and gas metallicities in the $Z = Z_\odot - 2Z_\odot$ range. Finally, the different black lines show the results from Equation (18) for the following set of conditions: $\sigma = 0$ and $n_e = 10$ cm^{-3} (solid line), $\sigma = 0$ and $n_e = 100$ cm^{-3} (dashed line), $\sigma = 0$ and $n_e = 800$ cm^{-3} (dot-dashed line), and $\sigma = 2$ and $n_{e0} = 100$ cm^{-3} (short-dashed line). Center: SFR versus L_{122}. We include for comparison the Farrah et al. (2013) sample of ULIRGs observed in [N II] 122 μm emission using *Herschel*/PACS. Open squares correspond to 3σ upper limits in L_{122}. The model and Equation (18) results are based on the same set of assumptions as those adopted in the first panel. Right: similar to the first two panels, but this time we plot the SFR versus the combined [N II] luminosity, $L_{122+205}$.

another factor that could play a role is the hardness of the ionizing radiation field, which controls the N^{++}/N^{+} ratio. Evidence for this comes from the observed systematic decrease in the L_{205}/L_{IR} ratio of star-forming galaxies and (U)LIRGs as the $L_{[O\,III]}/L_{205}$ ratio increases (Zhao et al. 2013). The $L_{[O\,III]}/L_{205}$ ratio should resemble the N^{++}/N^{+} ratio, as the energy needed to form N^{++} is only ~6 eV higher than that needed to form O^{++}. This analysis reinforces our previous conclusion about the limitations on using the [N II] 205 μm line as a star-formation tracer when the properties of the ionized gas of the source (in particular, n_e, σ, the ionization parameter, and the hardness of the radiation field) are not constrained.

Compared to the [N II] 205 μm case, the observed correlations for the BtP galaxies that involve the [N II] 122 μm line are tighter, resulting from a weaker dependence of the [N II] 122 μm line emission with electron density. This result is consistent with the predictions from the MAPPINGS-III code, where, for example, the SFR/L_{122} ratios for the $n_e = 10$ and 100 cm^{-3} cases only differ by a factor of 1.5. Similarly, the results from Equation (18) for $\sigma = 0$ and $n_e = 10$ and 100 cm^{-3} differ only by a factor of 1.2. Regarding the ULIRGs drawn from the Farrah et al. (2013) sample, they tend to have SFR/L_{122} ratios that are a factor of ~3 higher than those of the BtP galaxies. According to the results from Equation (18), this difference between the BtP galaxies and the LIRGs suggests that the ionized gas in the latter is dominated by dissimilar conditions, for example, a homogeneous ionized medium with a high electron density ($n_e = 800$ cm^{-3}), or ionized gas with $n_{e0} = 100$ cm^{-3} but characterized by a wide electron density distribution ($\sigma = 2$). Similar to the case of the (U)LIRGs in the Zhao et al. (2013) sample, one additional factor that needs to be considered is the increase in the N^{++}/N^{+} ratio with the hardness of the ionizing radiation field. In particular, Seyfert 2 galaxies and ULIRGS in the Farrah et al. (2013) sample that show weak polycyclic aromatic hydrocarbon emission (probably a sign of intense radiation fields) likely have hard radiation fields and $G_0/n_e \approx 10$ cm^3. These conditions place those galaxies in the regime where N^{++} is the dominant ionization stage (Abel et al. 2009), which may explain the observed high SFR/L_{122} ratios compared to those measured in the BtP sample.

In summary, we find that a [N II]-based SFR calibration (Equation (18)) depends, among other things, on the electron density of the gas, the shape of the electron density distribution, the hardness of the radiation field, and the nitrogen abundance. Additional constraints on the properties of the ionized gas, provided for example by the combination of the [N II] and [S III] lines, are required to avoid uncertainties in the SFR determinations larger than a factor of ~2. Without prior knowledge on these variables, the [N II] 122 μm transition is a slightly more reliable tracer than the [N II] 205 μm line because of its approximately six times higher critical density.

5. SUMMARY AND CONCLUSIONS

In this paper we use the [N II] 122 and 205 μm far-infrared transitions to study the properties of the low-excitation H II gas in 21 galaxies observed by *Herschel* as part of the "BtP" and KINGFISH projects. In particular, we use the [N II] 122/205 line ratio to measure the electron density of the low-excitation H II gas. We then study the dependence between the electron density and the properties of the ISM such as radiation field strength, infrared color, and metallicity. The [N II] 122 and 205 μm far-infrared lines also have potential as star-formation tracers, and in this work we study the correlations between the [N II] 122 and 205 μm emission and the star-formation activity. In particular, we explore the dependence of these correlations

with properties of the ionized gas such as its density and metallicity.

We highlight the following points:

1. For 141 regions selected from 21 galaxies, we measure [N II] 122/205 line ratios in the range ∼0.6–6, which correspond to electron densities of the photoionized gas in the range $n_e \sim 3-300\,\mathrm{cm}^{-3}$ (assuming a single n_e within each region). If we consider instead a distribution of electron densities that follows a log-normal distribution characterized by a width σ and a characteristic electron density n_{e0} (Equation (13)), then the relationship between the [N II] 122/205 line ratio and n_{e0} is given by Equation (15). We find that only one region has a [N II] 122/205 line ratio below the theoretical limit of ∼0.6, which corresponds to gas with $n_e \ll n_{crit}$. The median ionized gas density in the sample is $n_e \approx 30\,\mathrm{cm}^{-3}$, comparable to the median electron density measured in the Carina nebula (Oberst et al. 2006, 2011). Within individual galaxies, we measure variations in the ionized gas density as high as a factor of ∼50. In general, the central ∼400 pc regions exhibit the highest electron densities in the galaxy, which is expected as they typically have the highest SFR surface densities.
2. We find a good correlation between electron density and infrared color ($\nu f_\nu(70\,\mu\mathrm{m})/\nu f_\nu(100\,\mu\mathrm{m})$), dust-weighted mean starlight intensity ($\langle U\rangle$), TIR surface density (Σ_{TIR}), and SFR surface density (Σ_{SFR}). The origin of these good correlations could be associated with (1) the evolutionary stage of the H II region, as young, compact H II regions will produce very intense radiation fields, or (2) the fact that dense H II regions are in pressure equilibrium with the surrounding neutral gas implies a high-density molecular gas environment that may lead to further star-formation activity.

   These relationships can also be useful when, in order to predict the [N II] 205 μm intensity from the [N II] 122 μm intensity (or vice versa), an electron density needs to be assumed. In particular, we provide an equation to estimate the electron density from the $\nu f_\nu(70\,\mu\mathrm{m})/\nu f_\nu(100\,\mu\mathrm{m})$ infrared color:

$$\log_{10}\left(\frac{n_e}{\mathrm{cm}^{-3}}\right) = 3.41 \times \log_{10}\left(\frac{\nu f_\nu(70)}{\nu f_\nu(100)}\right) + 1.68.$$

3. We use the [N II] far-infrared transitions to measure the ionizing photon rate Q_0. In the low-density limit (Equation (8)) we use the observed [N II] 205 μm observations to estimate a median global ionizing photon rate $Q_0 = 1.98 \times 10^{52}\,\mathrm{s}^{-1}$ for the BtP galaxies. Because collisional deexcitation has been neglected, this is only a lower bound on Q_0. Normalized by the covered area, the median ionizing photon rate surface density is $1.96 \times 10^{51}\,\mathrm{s}^{-1}\,\mathrm{kpc}^{-2}$, which is ∼3 times the ionizing photon rate measured inside the solar circle (∼8.5 kpc) in the Milky Way (Bennett et al. 1994).
4. We derive relations between the [N II] line emission and SFR in the low-density limit (Equations (10) and (11)) and for distributions of electron densities (Equations (17) and (18)). The latter assumes a log-normal distribution of electron densities characterized by the width of the distribution σ ($\sigma = 0$ corresponds to uniform density) and the characteristic electron density of the ionized gas n_{e0}. We then relate the SFR and the [N II] luminosity via the calibration coefficient C (Equation (17)), which is the number of ionizing photons per erg of emitted energy in the [N II] lines; C is a function of the [N II] 122/205 line ratio (or electron density) and σ. We find that C increases as a function of both the [N II] 122/205 line ratio and the density distribution parameter σ. The differences between the values of C for different ionized gas conditions can be significant and imply that not only the [N II] 122/205 line ratio but also additional constraints on the electron density distribution are important to accurately measure SFRs based on the [N II] transitions.
5. In general, we find good correlations between the surface brightness of the [N II] line emission and the SFR surface density. However, and as we show in Equation (18), these correlations depend on the nitrogen abundance, the characteristic electron gas density, and the density distribution parameter σ. The lack of constraints on any of these parameters can result in large uncertainties in the SFR determination based on the [N II] lines only. The best linear fit to the observed correlations of Σ_{SFR} with Σ_{205}, Σ_{122}, and $\Sigma_{122+205}$ for the BtP regions are

$$\begin{aligned}\frac{\Sigma_{\mathrm{SFR}}}{M_\odot\,\mathrm{yr}^{-1}\,\mathrm{kpc}^{-2}} &= 4.51 \times 10^{-7}\left(\frac{(\mathrm{N/H})_\odot}{\mathrm{N}^+/\mathrm{H}^+}\right)\frac{\Sigma_{205}}{L_\odot\,\mathrm{kpc}^{-2}},\\ &= 3.33 \times 10^{-7}\left(\frac{(\mathrm{N/H})_\odot}{\mathrm{N}^+/\mathrm{H}^+}\right)\frac{\Sigma_{122}}{L_\odot\,\mathrm{kpc}^{-2}},\\ &= 3.31 \times 10^{-7}\left(\frac{(\mathrm{N/H})_\odot}{\mathrm{N}^+/\mathrm{H}^+}\right)\frac{\Sigma_{122+205}}{L_\odot\,\mathrm{kpc}^{-2}}.\end{aligned}$$

   For all three correlations, we find that regions with warm infrared colors tend to show deviations from the best linear fit in the sense that a [N II]-based SFR calibration will underestimate the reference amount of star-formation activity (measured as a combination of 24 μm and Hα emission). For the [N II] 205 μm line, these deviations starts at an IR color threshold of $\nu f_\nu(70\,\mu\mathrm{m})/\nu f_\nu(100\,\mu\mathrm{m}) \approx 0.9$, and they increase as a function of $\nu f_\nu(70\,\mu\mathrm{m})/\nu f_\nu(100\,\mu\mathrm{m})$ and n_e until reaching deviations of ∼1 dex at $\nu f_\nu(70\,\mu\mathrm{m})/\nu f_\nu(100\,\mu\mathrm{m}) \approx 1.2$. This is primarily a density effect, given that in regions with gas densities close to or greater than n_{crit}, the [N II] 205 μm collisional deexcitations compete with the radiative decays, and the [N II] 205 μm intensity stops tracing any increment in the star-formation activity. However, it is probably in part also due to ionization of N^+ to N^{++} and N^{+++} in high-density H II regions ionized by early-type O stars.

   For the two correlations that involve the [N II] 122 μm line, we also observe deviations from the best linear fit growing with IR color, but at a higher IR color threshold than in the [N II] 205 μm case ($\nu f_\nu(70\,\mu\mathrm{m})/\nu f_\nu(100\,\mu\mathrm{m} \approx 1.1$). This is because the critical density of the [N II] 122 μm transition is about six times higher than that of [N II] 205 μm, which makes the [N II] 122 μm transition less sensitive to the effects of density than the [N II] 205 μm line.
6. We compare the $L_{[\mathrm{N\,II}]}$–SFR correlations for the BtP galaxies to a sample of local (U)LIRGs (Farrah et al. 2013; Zhao et al. 2013) and predictions from the MAPPINGS-III photoionization code and Equation (18)

for different assumptions on the ionized gas properties. In general, we find good agreement between the $L_{[\mathrm{N\,II}]}$–SFR correlations and the model results, where the observed trends and scatter can be understood in terms of variations of the electron density of the gas and the width of the electron density distribution. Both theory and observations reveal the importance of having prior knowledge of the ionized gas properties of the source (e.g., metallicity, [N II] and [S III] based electron density measurements, ionization parameter) in order to avoid underestimating the star-formation activity. In case there are no constraints on the ionized gas, the [N II] 122 μm emission could be a slightly more reliable tracer than [N II] 205 μm because of its higher critical density.

The study of the [N II]-based SFR calibrations presented in this paper may prove useful in characterizing high-redshift ($z \gtrsim 2$) galaxies observed by ALMA. As we discussed in Section 5, this should be done carefully, as the [N II]-based SFR calibration depends on the nitrogen abundance, the electron density, the shape of the electron density distribution, and the ionization state of the gas. In the case there are additional tracers that can be used to measure the SFR (e.g., L_{FIR}), the comparison to the [N II]-based SFR measurement could be used to constrain the properties of the ionized gas of the system.

We thank the anonymous referee for helpful suggestions that improved the paper. RHC acknowledges support from a Fulbright-CONICYT grant. ADB acknowledges partial support from a CAREER grant NSF-AST0955836, from NASA-JPL 1373858, NSF-AST 1412419, and from a Research Corporation for Science Advancement Cottrell Scholar award. Beyond the Peak research has been supported by a NASA/JPL grant (RSA 1427378). JDS gratefully acknowledges visiting support from the Alexander von Humboldt Foundation and the Max Planck Institute für Astronomie. FST acknowledges financial support from the Spanish Ministry of Economy and Competitiveness (MINECO) under grant number AYA2013-41243-P. PACS has been developed by a consortium of institutes led by MPE (Germany) and including UVIE (Austria); KU Leuven, CSL, IMEC (Belgium); CEA, LAM (France); MPIA (Germany); INAF-IFSI/OAA/OAP/OAT, LENS, SISSA (Italy); IAC (Spain). This development has been supported by the funding agencies BMVIT (Austria), ESA-PRODEX (Belgium), CEA/CNES (France), DLR (Germany), ASI/INAF (Italy), and CICYT/MCYT (Spain). HIPE is a joint development by the Herschel Science Ground Segment Consortium, consisting of ESA, the NASA Herschel Science Center, and the HIFI, PACS, and SPIRE consortia. SPIRE has been developed by a consortium of institutes led by Cardiff University (UK) and including Univ. Lethbridge (Canada); NAOC (China); CEA, LAM (France); IFSI, Univ. Padua (Italy); IAC (Spain); Stockholm Observatory (Sweden); Imperial College London, RAL, UCL-MSSL, UKATC, Univ. Sussex (UK); and Caltech, JPL, NHSC, Univ. Colorado (USA). This development has been supported by national funding agencies: CSA (Canada); NAOC (China); CEA, CNES, CNRS (France); ASI (Italy); MCINN (Spain); SNSB (Sweden); STFC, UKSA (UK); and NASA (USA). This work is based (in part) on observations made with *Herschel*, a European Space Agency Cornerstone Mission with significant participation by NASA. This research has made use of the NASA/IPAC Extragalactic Database (NED), which is operated by the Jet Propulsion Laboratory, California Institute of Technology, under contract with the National Aeronautics and Space Administration.

REFERENCES

Abel, N. P., Dudley, C., Fischer, J., Satyapal, S., & van Hoof, P. A. M. 2009, ApJ, 701, 1147
Aniano, G., Draine, B. T., Calzetti, D., et al. 2012, ApJ, 756, 138
Aniano, G., Draine, B. T., Gordon, K. D., & Sandstrom, K. 2011, PASP, 123, 1218
Armus, L., Mazzarella, J. M., Evans, A. S., et al. 2009, PASP, 121, 559
Asplund, M., Grevesse, N., Sauval, A. J., & Scott, P. 2009, ARA&A, 47, 481
Beirão, P., Armus, L., Helou, G., et al. 2012, ApJ, 751, 144
Bennett, C. L., Fixsen, D. J., Hinshaw, G., et al. 1994, ApJ, 434, 587
Berkhuijsen, E. M., & Fletcher, A. 2008, MNRAS, 390, L19
Brauher, J. R., Dale, D. A., & Helou, G. 2008, ApJS, 178, 280
Calzetti, D., Kennicutt, R. C., Engelbracht, C. W., et al. 2007, ApJ, 666, 870
Combes, F., Rex, M., Rawle, T. D., et al. 2012, A&A, 538, L4
Cora, S. A. 2006, MNRAS, 368, 1540
Croxall, K. V., Smith, J. D., Brandl, B. R., et al. 2013, ApJ, 777, 96
Croxall, K. V., Smith, J. D., Wolfire, M. G., et al. 2012, ApJ, 747, 81
Dale, D. A., Aniano, G., Engelbracht, C. W., et al. 2012, ApJ, 745, 95
Dale, D. A., Cohen, S. A., Johnson, L. C., et al. 2009a, ApJ, 703, 517
Dale, D. A., Smith, J. D. T., Schlawin, E. A., et al. 2009b, ApJ, 693, 1821
De Looze, I., Cormier, D., Lebouteiller, V., et al. 2014, A&A, 568, A62
de Vaucouleurs, G., de Vaucouleurs, A., Corwin, H. G., Jr., et al. 1991, Third Reference Catalogue of Bright Galaxies, Vol. I, II, III (Berlin: Springer)
Decarli, R., Walter, F., Carilli, C., et al. 2014, ApJL, 782, L17
Decarli, R., Walter, F., Neri, R., et al. 2012, ApJ, 752, 2
Draine, B. T. 2011, ApJ, 732, 100
Draine, B. T., & Li, A. 2007, ApJ, 657, 810
Farrah, D., Lebouteiller, V., Spoon, H. W. W., et al. 2013, ApJ, 776, 38
Ferkinhoff, C., Brisbin, D., Nikola, T., et al. 2011, ApJL, 740, L29
Ferkinhoff, C., Brisbin, D., Nikola, T., et al. 2015, ApJ, 806, 260
Fischer, J., Sturm, E., González-Alfonso, E., et al. 2010, A&A, 518, L41
Franco, J., Kurtz, S. E., García-Segura, G., & Hofner, P. 2000, Ap&SS, 272, 169
Galametz, M., Kennicutt, R. C., Calzetti, D., et al. 2013, MNRAS, 431, 1956
Galavis, M. E., Mendoza, C., & Zeippen, C. J. 1997, A&AS, 123, 159
Goldsmith, P. F., Yıldız, U. A., Langer, W. D., & Pineda, J. L. 2015, ApJ, 814, 133
Graciá-Carpio, J., Sturm, E., Hailey-Dunsheath, S., et al. 2011, ApJL, 728, L7
Griffin, M. J., Abergel, A., Abreu, A., et al. 2010, A&A, 518, L3
Groves, B. A., Dopita, M. A., & Sutherland, R. S. 2004, ApJS, 153, 9
Herrera-Camus, R., Bolatto, A. D., Wolfire, M. G., et al. 2015, ApJ, 800, 1
Hill, A. S., Benjamin, R. A., Kowal, G., et al. 2008, ApJ, 686, 363
Ho, L. C., Filippenko, A. V., & Sargent, W. L. W. 1997, ApJS, 112, 315
Houck, J. R., Roellig, T. L., Van Cleve, J., et al. 2004, Proc. SPIE, 5487, 62
Hudson, C. E., & Bell, K. L. 2004, yCat, 343, 725
Hudson, C. E., & Bell, K. L. 2005, A&A, 436, 1131
Hughes, T. M., Baes, M., Fritz, J., et al. 2014, A&A, 565, A4
Hughes, T. M., Baes, M., Schirm, M. R. P., et al. 2016, A&A, 587, A45
Hunt, L. K., Draine, B. T., Bianchi, S., et al. 2014, A&A, 576, A33
Kennicutt, R. C., Bendo, G., Engelbracht, C., et al. 2003, American Astronomical Society Meeting 204, Abstract #33.04
Kennicutt, R. C., Calzetti, D., Aniano, G., et al. 2011, PASP, 123, 1347
Kewley, L. J., & Dopita, M. A. 2002, ApJS, 142, 35
Kewley, L. J., Dopita, M. A., Sutherland, R. S., Heisler, C. A., & Trevena, J. 2001, ApJ, 556, 121
Kobulnicky, H. A., & Kewley, L. J. 2004, ApJ, 617, 240
Langer, W. D., Goldsmith, P. F., Pineda, J. L., et al. 2015, A&A, 576, A1
Leitherer, C., Schaerer, D., Goldader, J. D., et al. 1999, ApJS, 123, 3
Leroy, A. K., Bigiel, F., de Blok, W. J. G., et al. 2012, AJ, 144, 3
Levesque, E. M., Kewley, L. J., & Larson, K. L. 2010, AJ, 139, 712
Luhman, M. L., Satyapal, S., Fischer, J., et al. 2003, ApJ, 594, 758
Makiwa, G., Naylor, D. A., Ferlet, M., et al. 2013, ApOpt, 52, 3864
Malhotra, S., Kaufman, M. J., Hollenbach, D., et al. 2001, ApJ, 561, 766
McKee, C. F., & Williams, J. P. 1997, ApJ, 476, 144
Moustakas, J., Kennicutt, R. C., Jr., Tremonti, C. A., et al. 2010, ApJS, 190, 233
Muñoz-Mateos, J. C., Gil de Paz, A., Boissier, S., et al. 2009, ApJ, 701, 1965
Murphy, E. J., Condon, J. J., Schinnerer, E., et al. 2011, ApJ, 737, 67
Nagao, T., Maiolino, R., De Breuck, C., et al. 2012, A&A, 542, L34
Oberst, T. E., Parshley, S. C., Nikola, T., et al. 2011, ApJ, 739, 100
Oberst, T. E., Parshley, S. C., Stacey, G. J., et al. 2006, ApJL, 652, L125
Orsi, Á, Padilla, N., Groves, B., et al. 2014, MNRAS, 443, 799

Parkin, T. J., Wilson, C. D., Schirm, M. R. P., et al. 2013, ApJ, 776, 65
Pellegrini, E. W., Smith, J. D., Wolfire, M. G., et al. 2013, ApJL, 779, L19
Pérez-Montero, E., & Contini, T. 2009, MNRAS, 398, 949
Petuchowski, S. J., Bennett, C. L., Haas, M. R., et al. 1994, ApJL, 427, L17
Pilyugin, L. S., & Thuan, T. X. 2005, ApJ, 631, 231
Poglitsch, A., Waelkens, C., Geis, N., et al. 2010, A&A, 518, L2
Redfield, S., & Falcon, R. E. 2008, ApJ, 683, 207
Regan, M. W., Sheth, K., Teuben, P. J., & Vogel, S. N. 2002, ApJ, 574, 126
Rigopoulou, D., Hurley, P. D., Swinyard, B. M., et al. 2013, MNRAS, 434, 2051
Rosenberg, M. J. F., van der Werf, P. P., Aalto, S., et al. 2015, ApJ, 801, 72
Storey, P. J., & Zeippen, C. J. 2000, MNRAS, 312, 813
Tayal, S. S. 2011, ApJS, 195, 12
Walter, F., Weiß, A., Riechers, D. A., et al. 2009, ApJL, 691, L1
Weingartner, J. C., & Draine, B. T. 2001, ApJS, 134, 263
Wright, E. L., Mather, J. C., Bennett, C. L., et al. 1991, ApJ, 381, 200
Wu, R., Madden, S. C., Galliano, F., et al. 2015, A&A, 575, A88
Wu, R., Polehampton, E. T., Etxaluze, M., et al. 2013, A&A, 556, A116
Zhao, Y., Lu, N., Xu, C. K., et al. 2013, ApJL, 765, L13
Zhao, Y., Lu, N., Xu, C. K., et al. 2016, ApJ, 819, 69